LJMU Research Online

Laskar, T, Eerten, HV, Schady, P, Mundell, CG, Alexander, KD, Duran, RB, Berger, E, Bolmer, J, Chornock, R, Coppejans, DL, Fong, WF, Gomboc, A, Jordana-Mitjans, N, Kobayashi, S, Margutti, R, Menten, KM, Sari, R, Yamazaki, R, Lipunov, VM, Gorbovskoy, E, Kornilov, VG, Tyurina, N, Zimnukhov, D, Podesta, R, Levato, H, Buckley, DAH, Tlatov, A, Rebolo, R and Serra-Ricart, M

 A Reverse Shock in GRB 181201A

http://researchonline.ljmu.ac.uk/id/eprint/11832/

Article

For more information please contact researchonline@ljmu.ac.uk

A Reverse Shock in GRB 181201A

Tanmoy Laskar[1], Hendrik van Eerten[1], Patricia Schady[1], C. G. Mundell[1], Kate D. Alexander[2,19],
Rodolfo Barniol Duran[3], Edo Berger[4], J. Bolmer[5], Ryan Chornock[6], Deanne L. Coppejans[2], Wen-fai Fong[2],
Andreja Gomboc[7], Núria Jordana-Mitjans[1], Shiho Kobayashi[8], Raffaella Margutti[2], Karl M. Menten[9], Re'em Sari[10],
Ryo Yamazaki[11], V. M. Lipunov[12,13], E. Gorbovskoy[13], V. G. Kornilov[12,13], N. Tyurina[13], D. Zimnukhov[13], R. Podesta[14],
H. Levato[15], D. A. H. Buckley[16], A. Tlatov[17], R. Rebolo[18], and M. Serra-Ricart[18]

[1] Department of Physics, University of Bath, Claverton Down, Bath, BA2 7AY, UK
[2] Center for Interdisciplinary Exploration and Research in Astrophysics (CIERA) and Department of Physics and Astronomy, Northwestern University, Evanston, IL 60208, USA
[3] Department of Physics and Astronomy, California State University, Sacramento, 6000 J Street, Sacramento, CA 95819, USA
[4] Department of Astronomy, Harvard University, 60 Garden Street, Cambridge, MA 02138, USA
[5] Max-Planck-Institut für extraterrestrische Physik, Giessenbachstraße, D-85748 Garching, Germany
[6] Astrophysical Institute, Department of Physics and Astronomy, 251B Clippinger Lab, Ohio University, Athens, OH 45701, USA
[7] Center for Astrophysics and Cosmology, University of Nova Gorica, Vipavska 13, 5000 Nova Gorica, Slovenia
[8] Astrophysics Research Institute, Liverpool John Moores University, IC2, Liverpool Science Park, 146 Brownlow Hill, Liverpool L3 5RF, UK
[9] Max-Planck-Institut für Radioastronomie, Auf dem Hügel 69, D-53121 Bonn, Germany
[10] Racah Institute of Physics, The Hebrew University, Jerusalem 91904, Israel
[11] Department of Physics and Mathematics, Aoyama-Gakuin University, Kanagawa 252-5258, Japan
[12] M. V. Lomonosov Moscow State University, Physics Department, Leninskie gory, GSP-1, Moscow, 119991, Russia
[13] M. V. Lomonosov Moscow State University, Sternberg Astronomical Institute, Universitetsky pr., 13, Moscow, 119234, Russia
[14] Observatorio Astronomico Felix Aguilar (OAFA), National University of San Juan, San Juan, Argentina
[15] Instituto de Ciencias Astronomicas, de la Tierra y del Espacio (ICATE), San Juan, Argentina
[16] South African Astronomical Observatory, P.O. Box 9, 7935 Observatory, Cape Town, South Africa
[17] Kislovodsk Solar Station of the Main (Pulkovo) Observatory, RAS, P.O. Box 45, ul. Gagarina 100, Kislovodsk, 357700, Russia
[18] Instituto de Astrofísica de Canarias (IAC), Calle Vía Láctea s/n, E-38200 La Laguna, Tenerife, Spain
Received 2019 July 30; revised 2019 August 14; accepted 2019 August 17; published 2019 October 17

Abstract

We present comprehensive multiwavelength radio to X-ray observations of GRB 181201A spanning from ≈ 150 s to ≈ 163 days after the burst, comprising the first joint ALMA–VLA–GMRT observations of a gamma-ray burst (GRB) afterglow. The radio and millimeter-band data reveal a distinct signature at ≈ 3.9 days, which we interpret as reverse-shock (RS) emission. Our observations present the first time that a single radio-frequency spectral energy distribution can be decomposed directly into RS and forward shock (FS) components. We perform detailed modeling of the full multiwavelength data set, using Markov Chain Monte Carlo sampling to construct the joint posterior density function of the underlying physical parameters describing the RS and FS synchrotron emission. We uncover and account for all discovered degeneracies in the model parameters. The joint RS–FS modeling reveals a weakly magnetized ($\sigma \approx 3 \times 10^{-3}$), mildly relativistic RS, from which we derive an initial bulk Lorentz factor of $\Gamma_0 \approx 103$ for the GRB jet. Our results support the hypothesis that low-density environments are conducive to the observability of RS emission. We compare our observations to other events with strong RS detections and find a likely observational bias selecting for longer lasting, nonrelativistic RSs. We present and begin to address new challenges in modeling posed by the present generation of comprehensive, multifrequency data sets.

Unified Astronomy Thesaurus concepts: Gamma-ray bursts (629); Astronomy data modeling (1859); High energy astrophysics (739); Transient sources (1851); Gamma-ray transient sources (1853); Radio transient sources (2008); X-ray transient sources (1852); Markov chain Monte Carlo (1889); Interstellar synchrotron emission (856); Shocks (2086); Relativistic jets (1390); Relativistic fluid dynamics (1389)

Supporting material: machine-readable tables

1. Introduction

Long-duration gamma-ray bursts, produced in the core collapse of massive stars, host the most energetic and most highly relativistic jets in the universe (Mészáros & Rees 1993; Rees & Mészáros 1994; Frail et al. 1997; Woosley & Bloom 2006). However, the nature of the central engine, as well as the mechanism by which these jets are launched and collimated, remain poorly understood (Mészáros 2006). Probing the nature of the central engine, such as magnetars or an accreting black hole, requires foremost determining the energetics and composition of the GRB jets themselves

(Metzger et al. 2011; Lyutikov & Camilo Jaramillo 2017). Unfortunately, the forward shock (FS) synchrotron "afterglow" emission, produced by the interaction of the jet with the environment, is insensitive to the properties of GRB jets; instead, the baryon content, initial bulk Lorentz factor, and magnetization of the ejecta can be studied by capturing emission from the reverse shock (RS), produced in the jet during its rapid deceleration by the ambient medium (Sari et al. 1998; Panaitescu & Kumar 2000; Granot & Königl 2003; Granot & Taylor 2005; Zhang & Kobayashi 2005).

Strong RSs are expected in ejecta where the magnetic field is dynamically unimportant, and the ratio of the magnetic energy density to the bulk kinetic energy $\sigma \lesssim 1$. On the other hand,

---

[19] NHFP Einstein Fellow.

highly magnetized outflows are expected to produce weak RS emission (Zhang & Kobayashi 2005; McMahon et al. 2006; Lyutikov & Camilo Jaramillo 2017). The expected signature of RS radiation comprises a characteristic synchrotron spectrum superposed on the afterglow emission (Kobayashi 2000), resulting in a flash beginning in the optical and typically lasting a few tens of seconds to minutes, and which rapidly cascades to radio frequencies, where it typically lasts a few days (Akerlof et al. 1999; Sari & Piran 1999a; Nakar & Piran 2004).

Recent multiwavelength observations have unequivocally isolated excess radio emission attributable to the RS, and a careful decomposition of the observed multifrequency (radio to X-ray) spectral energy distribution (SED) at different epochs into FS and RS contributions has allowed the first inferences of the Lorentz factor and magnetization of GRB jets (Laskar et al. 2013, 2016, 2018a, 2018c; Perley et al. 2014; van der Horst et al. 2014; Alexander et al. 2017). These works have usually provided point estimates on the RS parameters with no uncertainty estimates, owing to limitations of the modeling process.

Here, we present multiwavelength observations of GRB 181201A spanning from ≈ 150 s to ≈ 163 days after the burst at 35 frequencies from 6×10^8 Hz to 3×10^{17} Hz, including the first joint Giant Meterwave Radio Telescope (GMRT), Karl G. Jansky Very Large Array (VLA), and Atacama Large Millimeter/submillimeter Array (ALMA) data set (Section 2). Our radio and millimeter-band observations reveal an RS spectral peak superposed on the FS emission, which we are able to decompose into RS and FS components in a single radio SED for the first time (Section 3), while using the optical and X-ray observations to constrain the nature of the circumburst environment. We fit the entire multiwavelength data set simultaneously to derive the properties of the RS and FS emission, and demonstrate that the two components are consistent with emission from a double-shock system (Section 4). We use this decomposition to derive the initial Lorentz factor and magnetization of the ejecta using full statistical modeling. We conclude with a detailed discussion of the results, placed in context of other GRBs with multiwavelength RS detections (Section 5). Unless otherwise stated, all uncertainties are reported at the 1σ level, and all magnitudes are in the AB system and not corrected for Galactic extinction. We employ the ΛCDM cosmological parameters of $\Omega_m = 0.31$, $\Omega_\Lambda = 0.69$, and $H_0 = 68$ km s^{-1} Mpc^{-1} throughout.

2. Observations and Data Analysis

GRB 181201A was discovered by the IBIS and ISGRI instruments on board the *INTEGRAL* satellite on 2018 December 1 at 02:38 UT (Mereghetti et al. 2018). The burst, which lasted ≈ 180 s, saturated the telemetry, and hence only a lower limit to its γ-ray flux is available from *INTEGRAL*. The GRB was also detected by the *Fermi* Large Area Telescope (LAT) beginning at 02:38:00 UT (Arimoto et al. 2018), by *Konus*-Wind at 02:39:52.36 UT with a burst duration of ≈ 172 s (Svinkin et al. 2018), and by *Astrosat* with a duration of $T_{90} \approx 19.2$ s (Khanam et al. 2018). We take the *Fermi* and *INTEGRAL* time as T_0 for this burst, and reference all times hereafter to this T_0. The time-averaged *Konus*-Wind spectrum in the 20 keV–10 MeV energy range can be fit with a Band model, with low-energy photon index $\alpha_\gamma = -1.25 \pm 0.05$, high-energy photon index $\beta = -2.73^{+0.11}_{-0.12}$, peak energy

$E_{\gamma,\text{peak}} = (152 \pm 6)$ keV, and a fluence of $(1.99 \pm 0.06) \times 10^{-4}$ erg cm^{-2} (Svinkin et al. 2018).

The optical afterglow was discovered in MASTER (Lipunov et al. 2010) Global Robotic Net observations (Podesta et al. 2018) 10 s after the *INTEGRAL* alert and later by the *Swift* UV/optical telescope (UVOT; Roming et al. 2005; Siegel & Cannizzo 2018). Spectroscopic observations with the Very Large Telescope at the European Southern Observatory yielded a redshift of $z = 0.450$ based on identification of the Mg II doublet (Izzo et al. 2018). At this redshift, the *Konus*-Wind spectrum implies an isotropic-equivalent γ-ray energy of $E_{\gamma,\text{iso}} = (1.20 \pm 0.04) \times 10^{53}$ erg, This value is consistent with the GRB E_{peak}–$E_{\gamma,\text{iso}}$ relation (Amati 2006), suggesting that the prompt γ-ray emission in GRB 181201A is typical among the GRB population.

2.1. X-Ray: Swift/XRT

The *Swift* X-ray Telescope (XRT; Burrows et al. 2005) began observing GRB 181201A 0.16 days after the burst and detected a fading X-ray afterglow at R.A. = $21^{\text{h}}17^{\text{m}}11\overset{s}{.}20$, decl. = $-12°37'50\overset{''}{.}9$ (J2000), with an uncertainty radius of $1\overset{''}{.}4$ (90% containment).[20] XRT continued observing the afterglow for 20 days in photon-counting mode. The GRB entered a Sun constraint for *Swift* at ≈ 21 days after the burst and was dropped from the *Swift* schedule. We obtained 4.4 ks of *Swift* ToO observations on 2019 April 7 (≈ 127 days), when it was visible again. The X-ray afterglow was weakly detected. The data were automatically calibrated using the XRT pipeline and incorporated into the online light curve. We use a photon index of $\Gamma_X \approx 1.77$ and an unabsorbed counts-to-flux conversion rate from the *Swift* website of 4.75×10^{-11} erg cm^{-2} ct^{-1} to convert the 0.3–10 keV count rate light curve[21] to flux density at 1 keV for subsequent analysis.

2.2. UV, Optical, and Near-IR

We derived aperture photometry from pipeline-processed UVOT images downloaded from the *Swift* data center[22] with the UVOTPRODUCT (v2.4) software. We used a circular source extraction region with a $3\overset{''}{.}5$ radius, followed by an aperture correction based on the standard $5''$ aperture for UVOT photometry (Poole et al. 2008). We present our UVOT measurements in Table 1.

Four MASTER-net observatories (MASTER-Kislovodsk, MASTER-IAC, MASTER-SAAO, and MASTER-OAFA) participated in rapid-response and follow-up observations of GRB 181201A, beginning with 10 s exposures at 02:40:30 UT on 2019 December 1, ≈ 150 s after the burst and 10 s after the *INTEGRAL* alert in the *BVRI* and Clear bands[23] (Podesta et al. 2018). The MASTER autodetection system (Lipunov et al. 2010, 2019) discovered a bright optical afterglow at R.A. = $21^{\text{h}}17^{\text{m}}11\overset{s}{.}20$, decl. = $-12°37'51\overset{''}{.}4$ (J2000) with unfiltered magnitude ≈ 13.2 mag (Vega). MASTER follow-up observations continued until ≈ 3 days after the burst. We carried out astrometry and aperture photometry (using a $\approx 2\overset{''}{.}5$ aperture radius) for observations taken at each telescope

---

[20] http://www.swift.ac.uk/xrt_positions/00020848/
[21] Obtained from the *Swift* website at http://www.swift.ac.uk/xrt_curves/00020848 and rebinned to a minimum signal-to-noise ratio per bin of 8.
[22] http://www.swift.ac.uk/swift_portal
[23] MASTER Clear-band (*CR*) magnitudes are best described by the ratio $CR = 0.8R + 0.2B$.

Table 1
Swift UVOT Observations of GRB 181201A

Midtime, Δt (days)	UVOT band	Flux Density (mJy)	Uncertainty (mJy)	Detection? (1 = Yes)
0.176	*uw2*	6.19×10^{-1}	2.92×10^{-2}	1
0.246	*uw2*	4.61×10^{-1}	2.17×10^{-2}	1
0.302	*uw2*	3.31×10^{-1}	1.88×10^{-2}	1
...	...	...		

(This table is available in its entirety in machine-readable form.)

separately, calibrated to six nearby SDSS reference stars. We verified our photometry by measuring the brightness of comparison stars with similar brightness to the afterglow, and incorporated the derived systematic calibration uncertainty into the photometric uncertainty (Troja et al. 2017; Lipunov et al. 2019).

We observed the afterglow of GRB 181201A with the Gamma-Ray Burst Optical/Near-Infrared Detector (GROND) on the MPI/ESO 2.2 m telescope in La Silla in Chile beginning 0.91 days after the burst in $g'r'i'z'JHK$ filters. We calibrated the data with tools and methods standard for GROND observations and detailed in Krühler et al. (2008). We performed aperture photometry calibrated against PanSTARRS field stars in the $g'r'i'z'$ filters and against the 2MASS catalog in JHK.

We observed the afterglow with the Ohio State Multi-Object Spectrograph (OSMOS; Martini et al. 2011) on the 2.4 m Hiltner telescope at MDM Observatory on 2018 December 4, with 120 s exposures each in the *BVRI* bands. We obtained two later epochs of imaging using the Templeton detector on the 1.3 m McGraw-Hill telescope on the nights of 2018 December 9 and 10, obtaining 4×300 s each in r' and i' bands. Observations on December 10 were taken at a high airmass of 1.91 and under poor seeing. We performed aperture photometry with a $2''$ aperture on the Hiltner and McGraw-Hill images, referenced to SDSS.

We obtained Liverpool Telescope (LT; Steele et al. 2004) imaging with the infrared/optical camera (IO:O) at ≈2.7 days, comprising 3×120 s exposures in $g'r'i'$ bands. We performed aperture photometry using the Astropy Photutils package (Bradley et al. 2016) calibrated to SDSS. We also collected all optical photometry for this event published in GCN circulars. We present our combined optical and NIR data set in Table 2.

2.3. Millimeter: ALMA

We obtained five epochs of ALMA Band 3 (3 mm) observations of GRB 181201A spanning 0.88 days to 29.8 days after the burst through program 2018.1.01454.T (PI: Laskar). The observations utilized two 4 GHz wide basebands centered at 91.5 and 103.5 GHz, respectively, in the first epoch, and at 90.4 and 102.4 GHz in subsequent epochs. One of J2258−2758, J2148+0657, and J2000−1748 was used for bandpass and flux density calibration, while J2131−1207 was used for complex gain calibration in all epochs. We analyzed the data using the Common Astronomy Software Application (CASA; McMullin et al. 2007), and the afterglow was well detected in all epochs. We performed one round of phase-only self-calibration in the first two epochs, where the

deconvolution residuals indicated the presence of phase errors. We list the results of our ALMA observations in Table 3.

2.4. Centimeter: VLA

We observed the afterglow using the VLA starting 2.9 days after the burst through programs 18A-088 and 18B-407 (PI: Laskar). We detected and tracked the flux density of the afterglow from 1.2 GHz to 37 GHz over multiple epochs until ≈164 days after the burst. We used 3C 48 as the flux and bandpass calibrator and J2131−1207 as the complex gain calibrator. Where phase errors appeared to be present after deconvolution, we performed phase-only self-calibration in epochs with sufficient signal-to-noise. The effect of self-calibration impacted the measured flux density by ≲15% and only at the highest frequencies (≳15 GHz). We carried out data reduction using CASA and list the results of our VLA observations in Table 3.

2.5. Meter: uGMRT

We observed the afterglow using the upgraded Giant Meterwave Radio Telescope (uGMRT) through program 35_065 (PI: Laskar) starting 12.5 days and 13.5 days after the burst in Bands 4 (center frequency 550 MHz) and 5 (center frequency 1450 MHz), respectively. The observations utilized the full 400 MHz bandwidth of the uGMRT Wide-band Backend (GWB) system. We used 3C 48 for bandpass and flux density calibration, and J2131−1207 for complex gain calibration. We carried out data reduction using CASA and list the results of our uGMRT observations in Table 3.

3. Basic Considerations

We now interpret the X-ray to radio afterglow observations in the context of synchrotron emission arising from electrons accelerated to a nonthermal power-law distribution, $N_{\gamma_e} \propto \gamma_e^{-p}$, in relativistic shocks produced by the interaction of the GRB jet with the circumburst environment (Sari et al. 1998). We assume the energy density of accelerated particles and that of the magnetic field downstream of the shock to be a fraction ϵ_e and ϵ_B, respectively, of the shock kinetic energy density for a given total ejecta kinetic energy, $E_{K,iso}$. The observed spectral energy distribution (SED) of each synchrotron component is described by three break frequencies (the self-absorption frequency, ν_a, the characteristic frequency, ν_m, and the cooling frequency, ν_c), and the flux density normalization, $F_{\nu,m}$ (Granot & Sari 2002). The evolution of these quantities with time depends upon the radial density profile of the circumburst medium, $\rho = AR^{-k}$, for which we consider two standard possibilities: a constant-density ($k = 0$, $A \equiv n_0 m_p$; ISM) model (Sari et al. 1998) and a wind-like ($k = 2$, $A \equiv 5 \times 10^{11}$g cm$^{-1}A_*$) environment (Chevalier & Li 2000). We compute the resulting synchrotron spectra using the weighting prescription described in Laskar et al. (2014) to generate smooth light curves at all observed frequencies.

3.1. Radio/Millimeter: Presence of Additional Component

One of the most striking features of GRB 181201A revealed by our VLA and ALMA observations is a spectral bump in the centimeter- to millimeter-band SED at 3.9 days (Figure 1). The feature spans 3–24 GHz and can be fit with a smoothly broken

Table 2
Optical and Near-IR Observations of GRB 181201A

Δt (days)	Observatory	Instrument	Filter	Frequency (Hz)	Flux Density (mJy)	Uncertainty (mJy)	Detection? 1 = Yes	Reference
1.81×10^{-3}	MASTER-OAFA	MASTER	CR	4.67×10^{14}	1.25×10^{1}	1.27×10^{-1}	1	This work
2.42×10^{-3}	MASTER-OAFA	MASTER	CR	4.67×10^{14}	2.85×10^{1}	1.58×10^{-1}	1	This work
3.46×10^{-1}	iTelescope	T31	R	4.67×10^{14}	6.52×10^{-1}	1.83×10^{-2}	1	Kong (2018)
...	...	...	...	...	...	...	...	...

Note. The data have not been corrected for Galactic extinction.

(This table is available in its entirety in machine-readable form.)

Table 3
Radio and Millimeter Observations of GRB 181201A

Telescope	Frequency (GHz)	Time (days)	Flux Density (mJy)	Uncertainty (μJy)
ALMA	97.5	0.885	3.41	23
ALMA	96.4	1.92	1.99	25
VLA	2.73	2.93	0.478	70
...	...	...	...	...

(This table is available in its entirety in machine-readable form.)
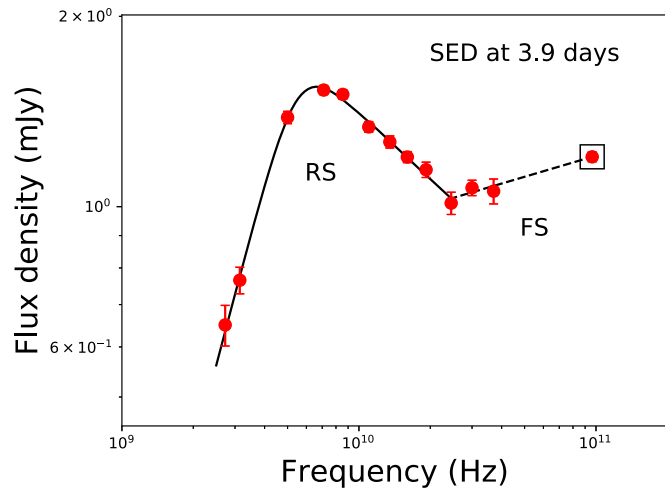
Figure 1. Radio and millimeter-band SED of GRB 181201A at 3.9 days postburst from our VLA and ALMA programs, with a broken power-law fit at 3–24 GHz (solid) and a single power law at high frequencies (dashed). The centimeter-band data spanning 3–24 GHz exhibit a self-absorbed spectral peak, which we attribute to emission from a reverse shock. The VLA observations above 24 GHz and the ALMA data (highlighted by a black box) constrain the high-frequency rising spectrum with index $\beta = 0.09 \pm 0.02$ and form a distinct emission component, which we associate with underlying forward shock emission (Section 3.1).

Figure 2. ALMA Band 3 (3 mm) light curve of GRB 181201A from ≈ 0.9 days to 30 days after the burst (blue circles) with a power-law model fit (blue line; $\alpha = -0.71 \pm 0.01$), along with VLA 16 GHz light curve (orange) and corresponding power-law fit for comparison. The steep light-curve decay indicates a wind-like pre-explosion environment (Section 3.2).

power law, with low-frequency index[24] $\beta_1 = 1.43 \pm 0.23$, high-frequency index $\beta_2 = -0.35 \pm 0.03$, break frequency $\nu_{peak} = 5.5 \pm 0.4$ GHz, and peak flux density $F_{\nu,peak} = 1.48 \pm 0.06$ mJy. The steeply rising spectrum below the spectral peak suggests the underlying emission is self-absorbed.[25] Fitting the VLA centimeter-band data above 24 GHz and the ALMA observations at the same epoch with a single power-law model yields $\beta_{24-ALMA} = 0.09 \pm 0.02$.

The radio and millimeter SED at 3.9 days clearly exhibits two distinct components. The simplest explanation for multiple components in the radio is to attribute one to an RS and the other to an FS. Because the RS emission is expected to peak at lower frequencies than the FS and the RS spectrum is expected to cut off steeply above the RS cooling frequency (Kobayashi 2000), the lower-peaking component is more naturally associated with RS emission.

The ALMA millimeter-band light curve can be fit with a single power law, with decay rate $\alpha_{ALMA} = -0.71 \pm 0.01$ (Figure 2). From the radio SED at 3.9 days, we know that $\nu_{m,f} > \nu_{ALMA}$ at this time. In this spectral regime, the expected rise rate for FS emission is $t^{1/2}$ in the ISM environment and t^0 in the wind environment, both of which are incompatible with the observed millimeter-band light curve. Thus, the millimeter-band light curve at <4 days originates from a separate component. The shallowest decline rate for an RS light curve at $\nu \gtrsim \nu_{m,r}$ is $\alpha \approx -2.1$ for a relativistic RS and $\alpha - 1.5$ for a nonrelativistic RS, in each case corresponding to a wind environment with $p \approx 2$. Both of these are steeper than the observed millimeter-band light curve. However, the sum of the contributions from the two emission components (RS and FS) may yield the observed shallower decay. We investigate this further in Section 5.2.

For the remainder of this article, we associate the low- and high-frequency components with emission from the RS and the

---
[24] We use the convention $F_\nu \propto t^\alpha \nu^\beta$ throughout.

[25] The deviation of this low-frequency power law from the expected value of $\beta \approx 2$ arises from a contribution from an underlying $\nu^{1/3}$ power law extending down from the millimeter band (Section 4).
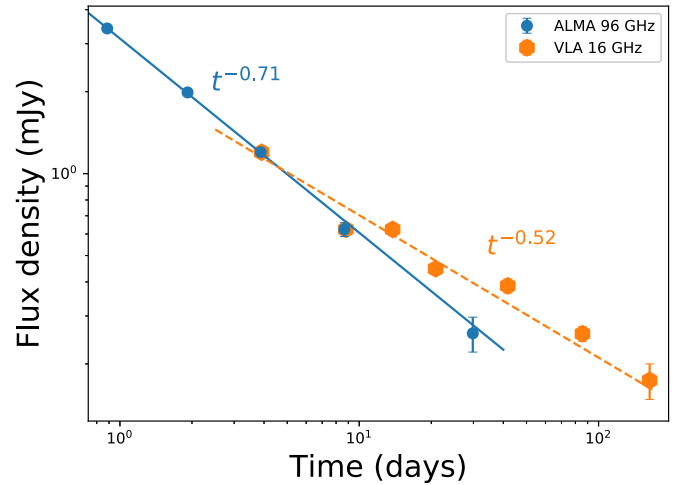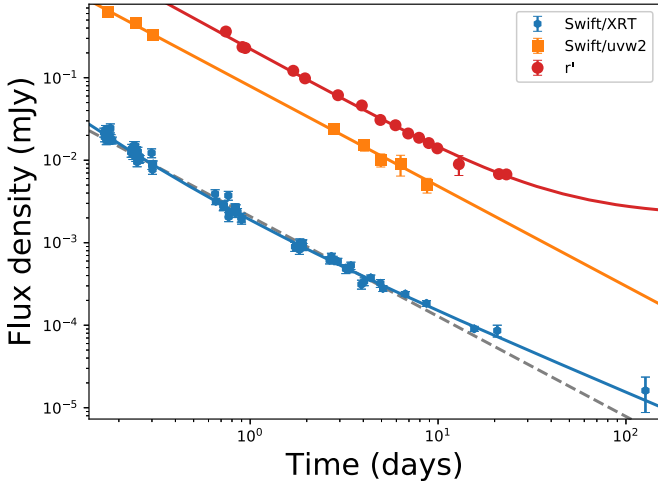
Figure 3. Optical r'-band, *Swift*/UVOT *uvw2*-band, and *Swift*/XRT 1 keV light curves of GRB 181201A, together with a power-law-plus-constant fit (red; r'-band), power-law fit at *uvw2*-band, and power-law (gray, dashed) and broken power-law fit (blue; X-ray). The excess emission in the r' band at $\gtrsim 10$ days may indicate contamination from the underlying host galaxy.

Figure 4. UV to X-ray SEDs at 0.9, 2.9, and 4.9 days, together with broken power-law model fits (lines). The spectral break suggests $\nu_{\rm opt} < \nu_{\rm c,f} < \nu_{\rm X}$ at this time (Section 3.2).

FS, respectively, and consider other scenarios in Section 5.5. In this framework, our observations of GRB 181201A provide the first instance where a single radio SED can be instantaneously and cleanly decomposed into RS and FS components, with the RS dominating at the lower frequency bands and the underlying FS emission clearly visible as an optically thin, rising spectrum at higher frequencies. We note that a more detailed characterization of these components, including the determination of the precise locations of their spectral break frequencies, requires a multiband model fit, which we undertake in Section 4.

3.2. Circumburst Density Profile

The identification of the FS component now allows us to constrain the circumburst density profile. We note that there is no evidence for a jet break until ≈ 21 days, as the X-ray light curve declines as a single power law from ≈ 0.15 days to ≈ 21 days ($\alpha_{\rm X} = -1.22 \pm 0.01$; Figure 3). The rising radio spectrum to ≈ 90 GHz at 3.9 days indicates that $\nu_{\rm m,f} \gtrsim 90$ GHz at this time. The relatively shallow spectral index of $\beta \approx 0.1$ compared to the expected index of $\beta = 1/3$ may result from the smoothness and potential proximity of the $\nu_{\rm m,f}$ break (Granot & Sari 2002).

Because $\nu_{\rm m,f} \gtrsim 90$ GHz at 3.9 days, the FS peak flux density $F_{\nu,\rm m,f} \gtrsim F_{\rm 3\,mm}(3.9\,{\rm days}) \approx 1.2$ mJy. In the ISM environment, this peak flux density, $F_{\rm p}$, remains fixed and must appear at a lower centimeter-band frequency, $\nu_{\rm cm}$, at a later time given by

$$ t_{\rm p} = \left(\frac{\nu_{\rm ALMA}}{\nu_{\rm cm}} \right)^{2/3} \left(\frac{F_{\rm p}}{F_{\rm ALMA}} \right)^2. \tag{1} $$

This implies a flux density of $F_{\rm p} \gtrsim 1.2$ mJy at $t_{\rm p} \gtrsim 13.2$ days at 16 GHz, which is a factor of 2 brighter than the observed 16 GHz light curve at the corresponding time. Indeed, all centimeter-band light curves are inconsistent with this extrapolation, and thus inconsistent with an ISM-like environment.

We now show that the optical to X-ray data are also inconsistent with an ISM environment and indicate a wind-like circumburst medium. The GROND SED at 0.91 days corrected
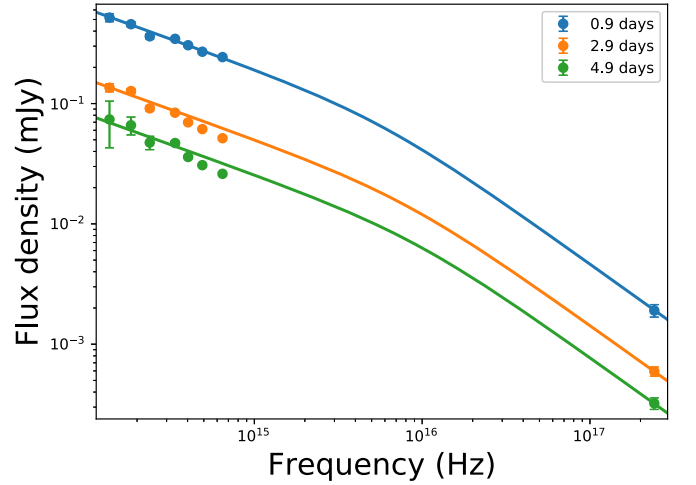
for a Galactic extinction of $A_{\rm V} = 0.17$ mag (Schlafly & Finkbeiner 2011) can be fit with a single power law, with index $\beta_{\rm opt} = -0.49 \pm 0.04$ (Figure 4). On the other hand, the spectral index between the GROND K-band and the X-rays is steeper, $\beta_{\rm NIR,X} = -0.75 \pm 0.02$, indicating that a spectral break lies between the optical/NIR and X-rays. The most natural explanation for these observations is $\nu_{\rm m,f} < \nu_{\rm opt} < \nu_{\rm c,f} < \nu_{\rm X}$. Fitting the optical and X-ray SED at 0.9 days, 2.9 days, and 4.9 days with broken power-law models[26] fixing the low-frequency index to $\beta_{\rm opt} = -0.5$ and the high-frequency index to $\beta_{\rm X} = -1.0$, we find a break frequency $\nu_{\rm b} = (5.7 \pm 1.5) \times 10^{15}$ Hz, $(8.1 \pm 2.0) \times 10^{15}$ Hz, and $(9.1 \pm 3.3) \times 10^{15}$ Hz, respectively (Figure 4). The rising break frequency is roughly consistent with the evolution of $\nu_{\rm c,f} \propto t^{1/2}$ in a wind-like environment. We caution that the inferred location of the break is only indicative, as it is degenerate with the spectral slopes and break smoothness.

For $\nu_{\rm m,f} < \nu_{\rm opt} < \nu_{\rm c}$, we expect a spectral index of $\beta = (1-p)/2$. Combined with the observed GROND SED at 0.9 days, this implies $p \approx 2$, which yields a light-curve decay rate of $\alpha_{\rm opt} \approx -1.25$ for the wind environment and $\alpha_{\rm opt} \approx -0.75$ for the ISM environment. The observed decay rate in the *Swift*/UVOT *uvw2*-band and in the ground-based optical r'-band observations at ≈ 0.2–8.7 days is $\alpha_{\rm UV} = -1.21 \pm 0.02$, consistent with the wind case and inconsistent with an ISM environment (Figure 3).

Above $\nu_{\rm c,f}$, we expect a decay rate of $\alpha = (2-3p)/4 \approx -1$. A power-law fit to the X-ray light curve yields a decay rate of $\alpha_{\rm X} = -1.212 \pm 0.013$; however, the light curve after ≈ 6 days is consistently above the single power-law fit. Adding a temporal break at $t_{\rm b} \approx 0.4$ days yields a better fit with $\alpha_{X,1} = -1.7 \pm 0.1$ and $\alpha_{X,2} = -0.96 \pm 0.02$. The steep early decay may imply that the cooling break is not far below the X-ray band, and we verify this with our full multiwavelength model in Section 4.1. On the other hand, the late-time excess is unusual, and we discuss this further in Section 5.3.

The measured X-ray photon index of $\Gamma_{\rm X} = 1.77 \pm 0.06$ implies $\beta_{\rm X} = -0.77 \pm 0.06$, which is not consistent with the

---

[26] $F_\nu = F_{\rm b} \left[\frac{1}{2} \left(\frac{\nu}{\nu_{\rm b}} \right)^{-y\beta_1} + \frac{1}{2} \left(\frac{\nu}{\nu_{\rm b}} \right)^{-y\beta_2} \right]^{-1/y}$. We fix $y = 3$ in this fit to emulate a moderately smooth break.

$\beta = -p/2 \approx -1$ expected for $p \approx 2$. We note that the Klein–Nishina (KN) correction may yield a spectral index of $\beta = -3(p-1)/4 \approx -0.75$ in some regimes (Nakar et al. 2009), and it is possible that this may impact the X-ray spectrum but not the light curve.[27] We defer a detailed discussion of the KN corrections to future work.

To summarize, the radio SED at 3.9 days and the millimeter-band light curve indicate the presence of an emission component separate from that responsible for the X-ray and optical emission. We interpret this low-frequency component as RS emission. Furthermore, we have described several observations that favor a wind-like circumburst environment: (i) the high millimeter-band flux density at 4 days that does not appear in the lower-frequency radio light curve, (ii) a slowly rising break between the optical and X-rays, and (iii) the optical light curve, which is consistent with $\nu_{m,f} < \nu_{opt} < \nu_c$ in a wind environment. We therefore focus on the wind environment in the remainder of this article.

3.3. Afterglow Onset

The first two MASTER observations at 156 and 209 s after the burst (156 s and 209 s, respectively) reveal a rapid brightening, $\alpha \approx 2.8$. Such brightenings have only been seen in a few other optical afterglows (Molinari et al. 2007; Liang et al. 2010; Melandri et al. 2010) and have been interpreted as the onset of the afterglow, where the increase in flux density corresponds to an ongoing transfer of energy from the ejecta to the FS, ultimately resulting in the deceleration of the ejecta (Rees & Mészáros 1992; Mészáros & Rees 1993; Kobayashi et al. 1999; Sari & Piran 1999b; Kobayashi & Zhang 2007). Unfortunately, our data do not capture the time of the peak in the optical bands. As the FS is not fully set up during this onset period, we do not include these points in our multiwavelength modeling (Section 4). We discuss these data further in Section 5.1.

4. Multiwavelength Modeling

4.1. Markov Chain Monte Carlo Analysis

Guided by the basic considerations discussed above, we fit all available X-ray to radio observations with a model comprising an FS and RS produced by a relativistic jet propagating in a wind-like circumburst environment. The free parameters for the FS model are p, $E_{K,iso,52}$, A_*, ϵ_e, ϵ_B, and the extinction A_V. Given the relatively shallow decline rate of the millimeter-band light curve ($\alpha \approx -0.72$) corresponding to the RS component, we focus on the nonrelativistic RS model, which allows for a shallower light-curve decay than a relativistic RS. The free parameters for the RS model[28] are the break frequencies $\nu_{a,r}$, $\nu_{m,r}$, $\nu_{c,r}$ and the RS peak flux, $F_{\nu,m,r}$ all at a reference time $t_{ref} \equiv 0.01$ days selected to be $\approx$few $\times$ T_{90} (and hence comparable to t_{dec}). Additionally, we allow the parameter g, corresponding to the evolution of the RS Lorentz factor with

radius after the deceleration time ($\Gamma \propto R^{-g}$), to vary (Mészáros & Rees 1999; Kobayashi & Sari 2000). Finally, we allow for a constant contribution to the light curves from an underlying host galaxy in bands where late-time flattening is evident (optical *griz* bands and the centimeter bands from 2.7 to 24.5 GHz). All free parameters, including RS and FS components and the underlying host galaxy contamination, are fit simultaneously. Further details of the modeling procedure, including the likelihood function employed, are described elsewhere (Laskar et al. 2013, 2014, 2016).

We performed a Markov Chain Monte Carlo (MCMC) exploration of the multidimensional parameter space using emcee (Foreman-Mackey et al. 2013). We ran 512 walkers for 10,000 steps and discarded a few ($\lesssim 0.15\%$) initial nonconverged steps with low log likelihood as burn-in. Our highest likelihood model with $p \approx 2.1$, $\epsilon_e \approx 0.37$ $\epsilon_B \approx 9.6 \times 10^{-3}$, $E_{K,iso} \approx 2.2 \times 10^{53}$ erg, $A_* \approx 1.9 \times 10^{-2}$, and negligible extinction, $A_V \lesssim 0.02$ mag, together with an RS model with $g \approx 2.7$, $\nu_{a,r} \approx 4.2$ GHz, $\nu_{c,r} \approx 90$ GHz, and $F_{\nu,a,r} \approx 0.6$ mJy at 3.9 days fits the X-ray to radio light curves and radio SEDs well (Figures 5 and 6). The peak in the centimeter-band spectrum at 3.9 days corresponds to $\nu_{a,r}$. The sum of the RS self-absorbed spectrum and the FS optically thin $\nu^{1/3}$ spectrum below $F_{\nu,a,r}$ (Figure 6) explains the intermediate $\beta \approx 1.4$ spectral index below the centimeter-band peak (Section 3.1). We present a selection of SEDs spanning radio to X-rays in Figure 7, and all light curves together in Figure 8.

For this model, the FS cooling frequency $\nu_{c,f} \approx 2.6 \times 10^{16}$ Hz at 1 day lies between the optical and X-rays, as expected from the basic considerations in Section 3.2. The proximity of $\nu_{c,f}$ to the X-ray band ($\nu_{c,f} \approx 0.3$ keV at 8 days) explains the moderately steep decline in the X-ray light curve, compared to the expectation for $\nu_X \gtrsim \nu_{c,f}$. Furthermore, $\nu_{a,f} \approx 60$ MHz is below the VLA and GMRT frequencies and is therefore not constrained, resulting in degeneracies between the model parameters (Figure 9). The FS characteristic frequency at 4 days, $\nu_{m,f} \approx 6 \times 10^{11}$ Hz, is above the ALMA band, as expected from the radio/millimeter SED at that time (Section 3.1). We list the properties of the best-fit model and summarize the marginalized posterior density function in Table 4.

4.2. Determination of Ejecta Initial Lorentz Factor

We now use the MCMC results to derive the initial Lorentz factor of the jet. The jet's initial Lorentz factor can be determined from joint RS and FS observations by solving the following equations self-consistently (Zhang et al. 2003; Laskar et al. 2018a) at the deceleration time, t_{dec},

$$\frac{\nu_{m,r}}{\nu_{m,f}} \sim \Gamma_0^{-2} R_B,$$
$$\frac{\nu_{c,r}}{\nu_{c,f}} \sim R_B^{-3},$$
$$\frac{F_{\nu,m,r}}{F_{\nu,m,f}} \sim \Gamma_0 R_B, \tag{2}$$

where Γ_0 is the initial Lorentz factor of the GRB jet, $R_B \equiv (\epsilon_{B,r}/\epsilon_{B,f})^{1/2}$ is the relative magnetization of the ejecta, and we have assumed similar values of ϵ_e and the Compton Y parameter in the two regions. The effective magnetizations of

---

[27] When $p \approx 2$, the effect of KN corrections on the evolution of ν_c with time, and hence on the light curve above ν_c, is small. However, the spectral corrections remain, and in particular, we may have $\nu_c < \hat{\nu}_c < \nu_X$, which would result in a spectral index of $\beta \approx -0.75$ (Nakar et al. 2009). Here $\hat{\nu}_c/\nu_c = (\hat{\gamma}_c/\gamma_c)^2$, $\hat{\gamma}_c = \gamma_{self}^3/\gamma_c^2$, $\gamma_{self} = (B_{QED}/B)^{1/3}$, B is the postshock magnetic field, and B_{QED} is the quantum critical field.

[28] We opt to fit for the observable quantities rather than the derived quantities of Γ_0, t_{dec}, and R_B for the RS, as these observables uniquely specify the RS spectrum independent of the FS parameters during the fitting process.
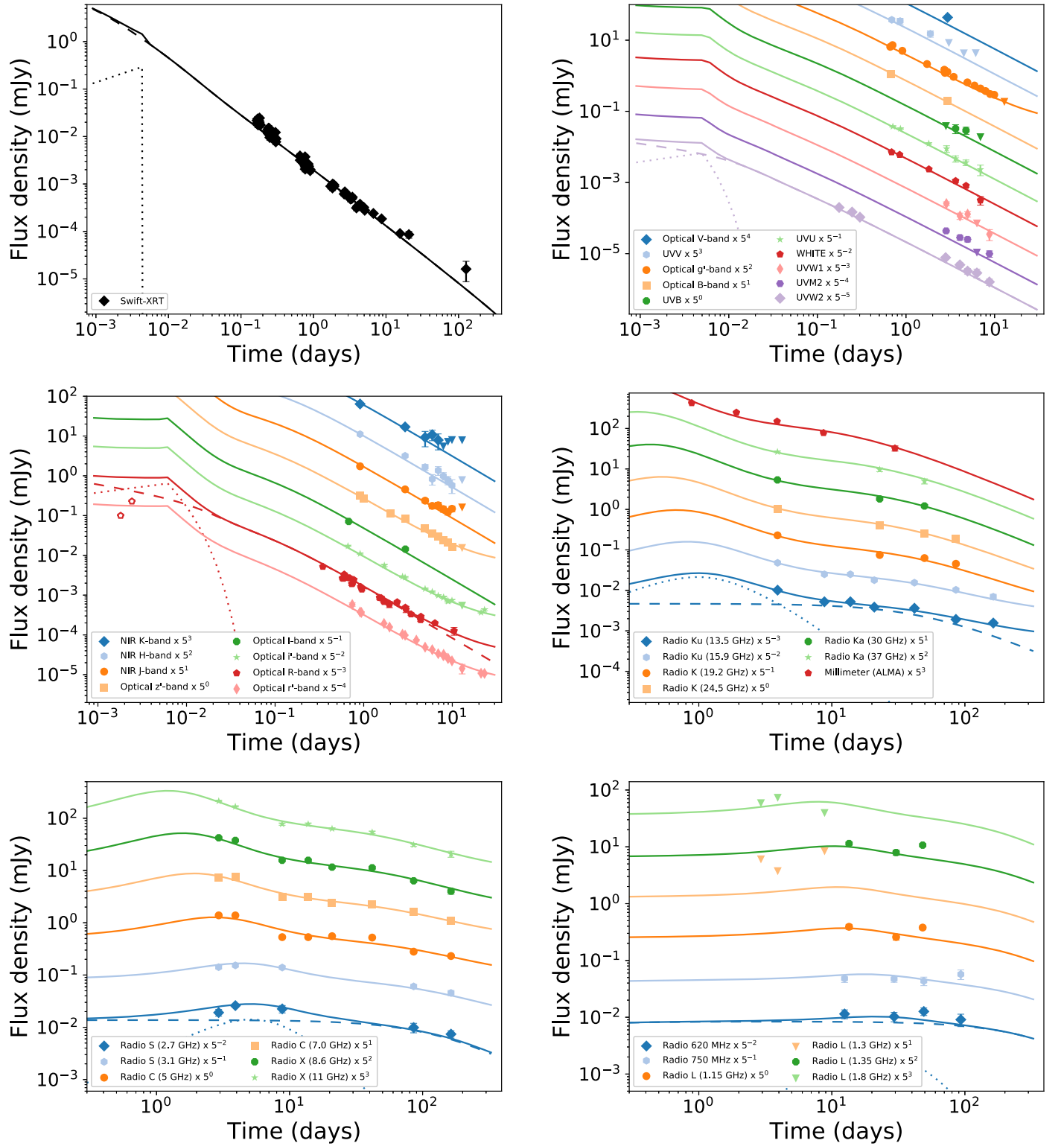
Figure 5. X-ray (top left), UV/optical (top right), optical/NIR (center left), and radio (center right and bottom) light curves of GRB 181201A, together with a full FS+RS model (solid lines). Data represented by open symbols are not included in the model fit. We show a decomposition of the X-ray, *Swift*/w2-band, optical *R*-band, 13.5 GHz, 2.7 GHz, and 620 MHz light curves into FS (dashed) and RS (dotted) components. Light curves exhibiting a late-time flattening incorporate a contribution from the underlying host galaxy (Section 4.1). The combined model explains the overall behavior of the light curves at all 36 observing frequencies. See Figure 8 for a combined plot showing all light curves together.

the shocked ejecta and shock external medium may well be very different, and the introduction of R_B allows us to investigate such variations caused, for instance, by the presence

of magnetic fields produced in the initial GRB and advected in the outflow (Usov 1992; Mészáros & Rees 1997; Zhang et al. 2003).
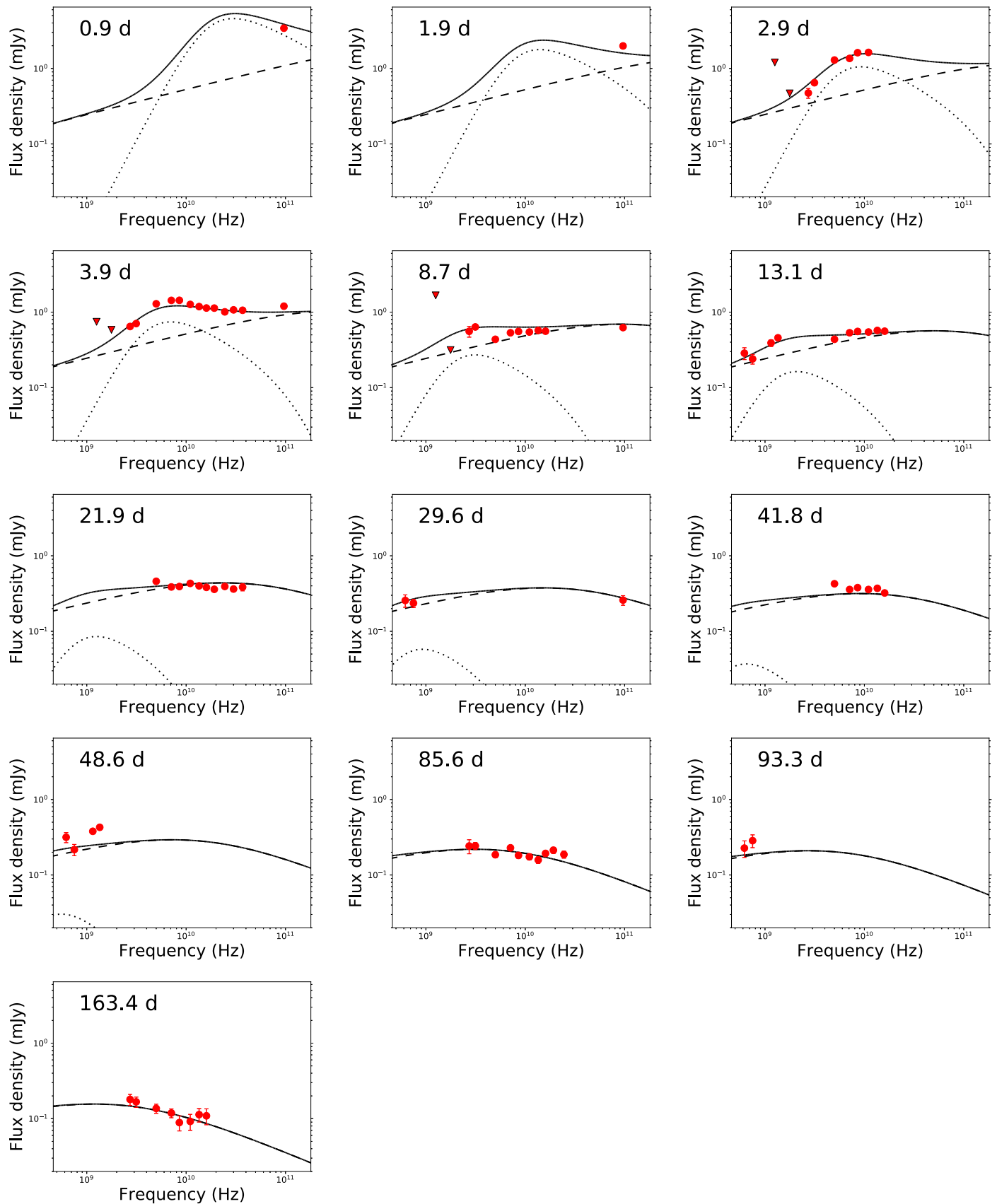
Figure 6. VLA centimeter-band and ALMA millimeter-band spectral energy distributions of GRB 181201A at multiple epochs starting at 0.9 days, together with the same FS+RS wind model as in Figure 5 (solid), decomposed into FS (dashed) and RS (dotted) contributions. The contribution of the host galaxy (included in the modeling) has been subtracted from the measured flux density at each frequency. See Figure 7 for a plot showing these SEDs together with optical and X-ray observations.
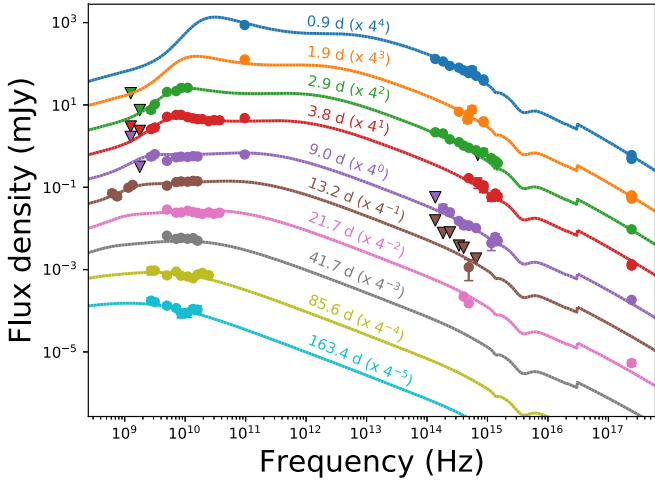
Figure 7. Multiband SEDs of GRB 181201A from ≈0.9 to ≈163.4 days, together with the FS+RS model presented in Section 4. The combined model explains the overall behavior of the afterglow spanning over eight orders of magnitude in frequency and over two orders of magnitude in time.

This system of equations has three unknowns (t_{dec}, R_B, and Γ_0) and can be inverted exactly to yield

$$t_{dec} = t_{ref}\left[\left(\frac{\nu'_{c,f}}{\nu'_{c,r}}\right)\left(\frac{F'_{\nu,m,f}}{F'_{\nu,m,r}}\right)^2\left(\frac{\nu'_{m,f}}{\nu'_{m,r}}\right)\right]^\tau,$$

$$\tau \equiv \left[\frac{15}{2(4-k)} - \frac{8(g+3)}{7(2g+1)}\right]^{-1} \quad (3)$$

where the primed quantities refer to values at the reference time of $t_{ref} = 0.01$ days used in the MCMC analysis. For our best-fit model, this yields $t_{dec} \approx 5.3 \times 10^{-3}$ days or ≈460 s; the full MCMC analysis gives $\log(t_{dec}/\text{days}) = -2.27^{+0.13}_{-0.14}$. We note that this is longer than the burst duration, $T_{90} \approx 172$ s (Section 2), consistent with the thin shell case (Zhang et al. 2003).

Given this value of t_{dec}, which satisfies Equation (2), we can in principle compute the initial Lorentz factor and magnetization,

$$R_B = \left(\frac{\nu_{c,f}}{\nu_{c,r}}\right)^{1/3}$$

$$\Gamma_0 = \frac{F_{\nu,m,r}}{F_{\nu,m,f}}R_B^{-1}. \quad (4)$$

However, we find that whereas $\nu_{c,r}$ and $\nu_{c,f}$ are reasonably well constrained, $F_{\nu,m,r}$ is completely degenerate with $\nu_{m,r}$. This is because the RS peak in the radio band corresponds to $\nu_{a,r}$, and hence the data do not constrain $\nu_{m,r}$. In the observed regime of $\nu_{m,r} < \nu_{a,r}$, the peak flux density of the RS component, $F_{\nu,a,r} \propto F_{\nu,m,r}(\nu_{a,r}/\nu_{m,r})^{(1-p)/2}$ results in the degeneracy, $F_{\nu,m,r} \propto \nu_{m,r}^{(1-p)/2} \propto \nu_{m,r}^{-0.5}$ for $p \approx 2$, which exactly explains the observed correlation between these parameters (Figure 9). Our MCMC samples span four orders of magnitude in $\nu_{m,r}$ and correspondingly about two orders of magnitude in $F_{\nu,m,r}$. The sampling is clipped at the lower end in $\nu_{m,r}$ by the prior on

$\nu_{m,r} > 10^8$ Hz (corresponding to $F_{\nu,m,r} \lesssim 10^8$ mJy) and at the lower end in $F_{\nu,m,r}$ by the actual observed peak flux density of the RS component (corresponding to $\nu_{m,r} \lesssim 10^{12}$ Hz). This degeneracy between $\nu_{m,r}$ and $F_{\nu,m,r}$ does not affect the calculation of t_{dec} (Equation (3)), because $\nu_{m,r}$ and $F_{\nu,m,r}$ enter in the combination $F_{\nu,m,r}\nu_{m,r}^2 \propto \nu_{m,r}^{2-p}$, which is only weakly dependent on $\nu_{m,r}$ for $p \approx 2$ (i.e., the degenerate terms cancel out). Therefore, we can constrain t_{dec} and R_B through this system of equations, but not Γ_0. We find $R_B \approx 0.65$ for the best-fit solution, and $R_B = 0.64^{+0.07}_{-0.08}$ from the MCMC.

To infer Γ_0 in this case, we turn to an energy balance argument (Zhang et al. 2003). At t_{dec}, the energy in the swept-up material (E_{sw}) is similar to the rest energy of the ejecta (which is the same as the explosion kinetic energy, E),

$$E_{sw} = \Gamma_0^2 M_{sw}c^2 \approx E, \quad (5)$$

where the swept-up mass at radius, R,

$$M_{sw} = \frac{4\pi AR^{3-k}}{3-k} \quad (6)$$

Combining Equations (5) and (6), the deceleration radius

$$R = \left[\frac{(3-k)E}{4\pi A\Gamma_0^2 c^2}\right]^{1/(3-k)} = \Gamma_0^{-2/(3-k)}l_{Sedov}, \quad (7)$$

where l_{Sedov} is the Sedov length, which depends only on the energy and density, parameters that are known from the FS modeling. For a point source moving along the line of sight, this radius corresponds to the deceleration time given by $R = 2\Gamma_0^2 ct_{dec}/(1+z)$, which gives the initial Lorentz factor

$$\Gamma_0 \approx \left[\frac{l_{Sedov}}{c}\left(\frac{2t_{dec}}{1+z}\right)\right]^{\frac{3-k}{2(4-k)}}. \quad (8)$$

We note that this is a simplified treatment, and a more rigorous analysis requires integrating over the full fluid profile and using the specific enthalpy of the shocked region while calculating the swept-up mass. However, for our purposes, this approximate expression will suffice to estimate Γ_0. We compute Γ_0 for all MCMC samples using Equation (8), resulting in $\Gamma_0 = 103^{+10}_{-8}$ (Figure 10).

5. Discussion

5.1. Early Optical Rise

We now return to the optical rise observed at $\lesssim 2.4 \times 10^{-3}$ days with MASTER (Figure 5). These observations were performed at $\lesssim t_{dec}$ in our best-fit RS+FS model (Section 4 and Table 4), consistent with the afterglow onset scenario. The spectral ordering at t_{dec} is $\nu_{m,r} < \nu_{a,r} < \nu_{opt} \approx \nu_{c,r}$ and $\nu_{a,f} < \nu_{c,f} < \nu_{opt} < \nu_{m,f}$. In this model, the RS light curve at $\lesssim t_{dec}$ is expected to rise at the rate $\alpha = (p-1)/2 \approx 0.5$, while the FS light curve should rise as $\alpha = 1/2$ (Zou et al. 2005). However, the observed rise of $\alpha \approx 2.8$ is not consistent with either prediction. The proximity of $\nu_{c,r}$ to ν_{opt} at the deceleration time may suppress the RS flux. On the other hand, the FS model also overpredicts the observed flux. One possible solution is the rapid injection of energy into the FS during
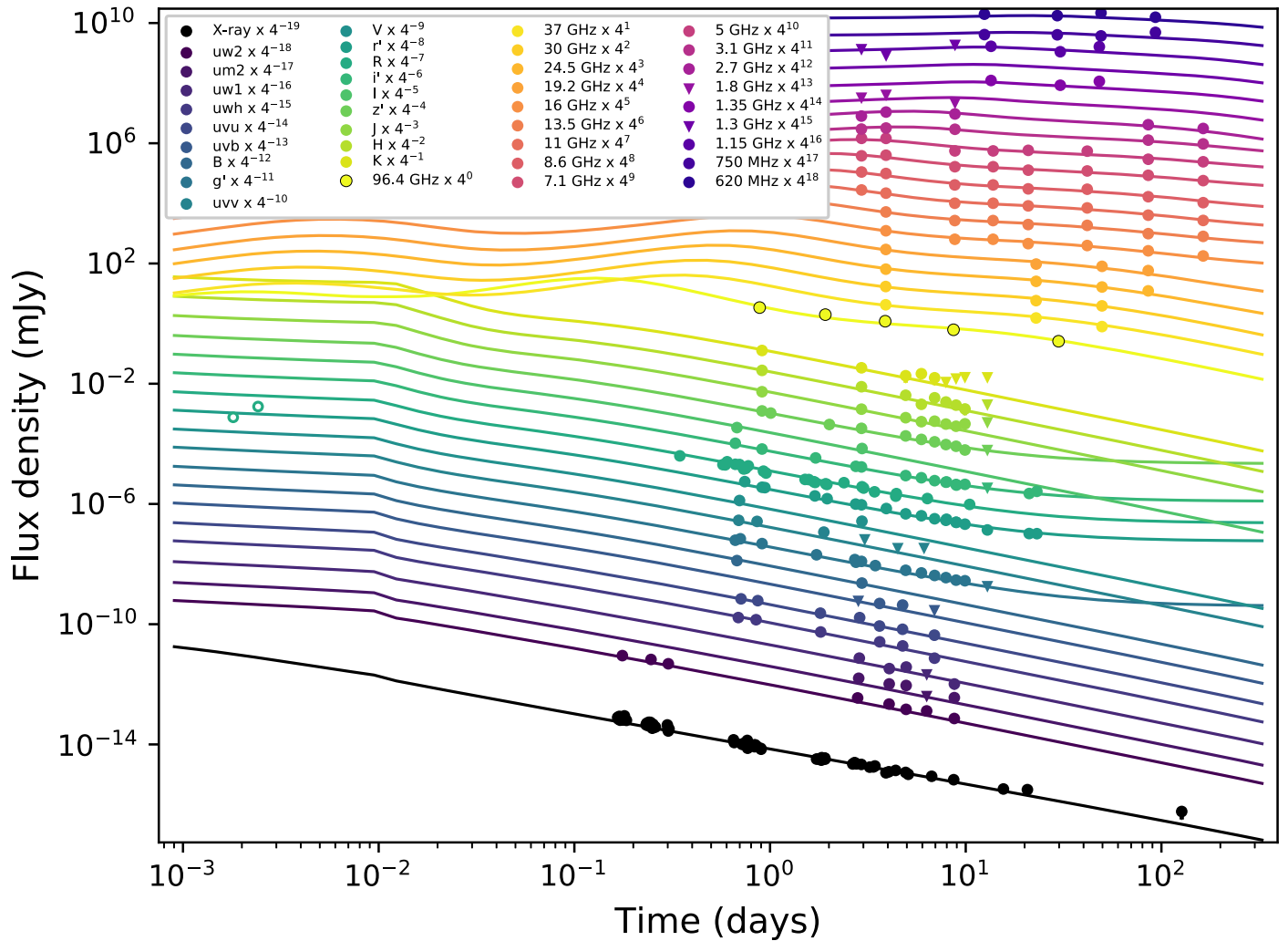
Figure 8. X-ray to radio light curves of GRB 181201A, together with the FS+RS model presented in Section 4, presented together for reference. The combined model explains the overall behavior of the light curves at all 36 observing frequencies.

this period. We find that an energy increase at the rate $E \propto t^{1.8}$ until $t_{\rm dec}$ roughly accounts for the optical rise[29] (Figure 11). Such an injection could arise, for instance, by the presence of energy at Lorentz factors $\lesssim \Gamma_0$ owing to velocity stratification in the ejecta (Sari & Mészáros 2000), which has previously been inferred in other GRB afterglows (Laskar et al. 2015, 2018a, 2018c). An alternate scenario could be a pair-dominated optical flash, as suggested for GRB 130427A (Vurm et al. 2014). However, the paucity of data around the optical peak precludes a more detailed analysis.

5.2. Intermediate Millimeter Excess

The 3 mm model light curve underpredicts two of the ALMA detections at ≈1.9 and ≈3.9 days by ≈20% (Figure 12). In particular, the observed light curve exhibits a shallower decline than afforded by the current model, where the transition between RS dominant to FS dominant at ≈1.5 days results in an inflection in the model light curve, which is not seen in the data. One possibility for a shallower RS decline rate is for the RS to be refreshed by slower ejecta catching up

with the FS (Sari & Mészáros 2000). This scenario requires a distribution of Lorentz factors in the jet, which has indeed been inferred in other events (Laskar et al. 2015, 2018c, 2018a) and remains feasible here. We note that a similar discrepancy was present in the only other ALMA light curve of a GRB available at this date, that of GRB 161219B (Laskar et al. 2018a). In that case, the model underpredicts the data at ≈3 days, corresponding to a similar RS–FS transition. These similarities may indicate that the RS evolution is more complex than previously thought, or that the millimeter-band emission is not dominated by the RS at all, and is in fact a separate component. Further ALMA 3 mm observations of GRBs, together with detailed multiwavelength modeling, may help shed light on this issue.

5.3. Late X-Ray Excess

The observed 1 keV light curve exhibits a late-time shallowing (Figure 3) and can therefore not be fit perfectly in our model (Figure 5), where only steepenings are expected (for instance, following a jet break; Sari et al. 1999). As a result, our best-fit model underpredicts the X-ray flux density at 127 days. Above $\nu_{\rm m,f}$, the afterglow light curves are indeed expected to become shallower at late times when the FS becomes nonrelativistic at $t_{\rm NR}$ (Waxman et al. 1998). One simple definition of $t_{\rm NR}$ corresponds to

---

[29] The FS dynamics during shock crossing for a shell with a uniform Γ_0 is equivalent to energy injection at the rate $E \propto t$ (Appendix B of Laskar et al. 2015).
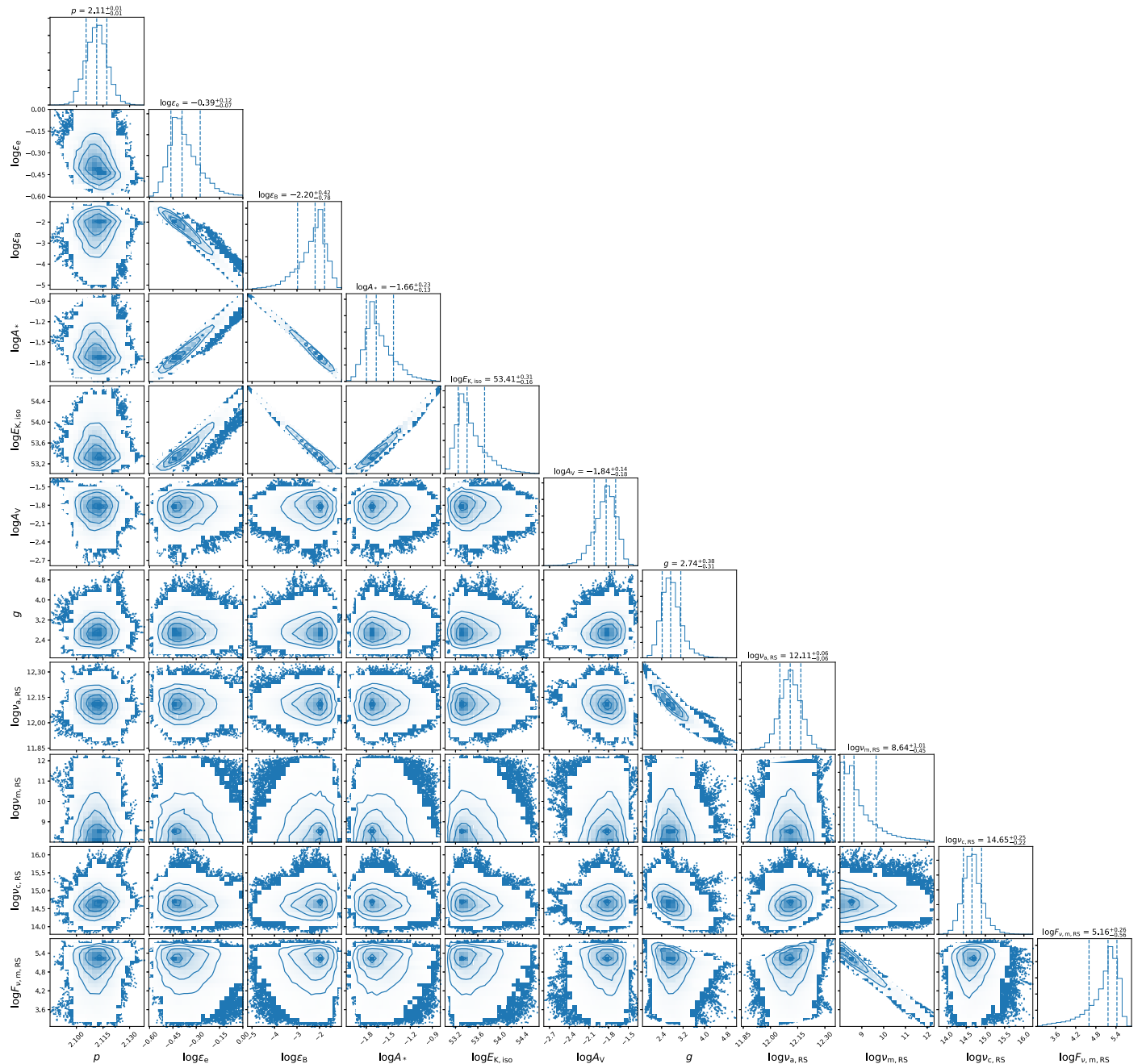
Figure 9. Correlations and marginalized posterior density for all free parameters in the RS+FS model (not including the host galaxy fluxes). Frequencies are in units of hertz, $F_{\nu,m,r}$ in mJy, and $E_{K,iso}$ in erg. The contours enclose 39.3%, 86.4%, and 98.9% of the probability mass in each correlation plot (corresponding to 1σ, 2σ, and 3σ regions for two-dimensional Gaussian distributions), while the dashed lines in the histograms indicate the 15.9%, 50% (median), and 84.1% quantiles (corresponding to $\pm 1\sigma$ for one-dimensional Gaussian distributions).

the time when $\Gamma\beta \approx 1$ (i.e., $\Gamma \approx \sqrt{2}$). For the best-fit model, these parameters correspond to $t_{NR} \approx 220$ yr, which cannot explain the X-ray excess at ≈ 127 days. Another possibility is that the late-time excess corresponds to a contaminating source within the XRT point-spread function, which has been observed at least once before; however, this possibility is quite rare and unlikely. One way to test this is to obtain observations of the afterglow with *Chandra*; however, at the time of writing, the target was within an extended Sun constraint for *Chandra* and not visible.

We note that late-time excess X-ray flux has been uncovered in other events (Fong et al. 2014; Margutti et al. 2015; Laskar et al. 2018b). Suggested explanations have included dust echoes, inverse-Compton scattering, late-time radiation from

the spin down of a magnetar central engine, and interaction of the FS with the shocked stellar wind at the edge of the stellar wind bubble (Shao & Dai 2007; Chandra et al. 2008; Liang et al. 2008; Mimica & Giannios 2011; Gat et al. 2013; Fong et al. 2014; Margutti et al. 2015). For reference, the shock radius at 127 days is ≈ 30 pc for our best-fit parameters, which is significantly larger than the mean distance between O stars in a typical massive stellar cluster (Figer et al. 1999).

5.4. Late Radio Excess

The 1–2 GHz GMRT light curves appear to exhibit an unexpected brightening of the afterglow between 30 and
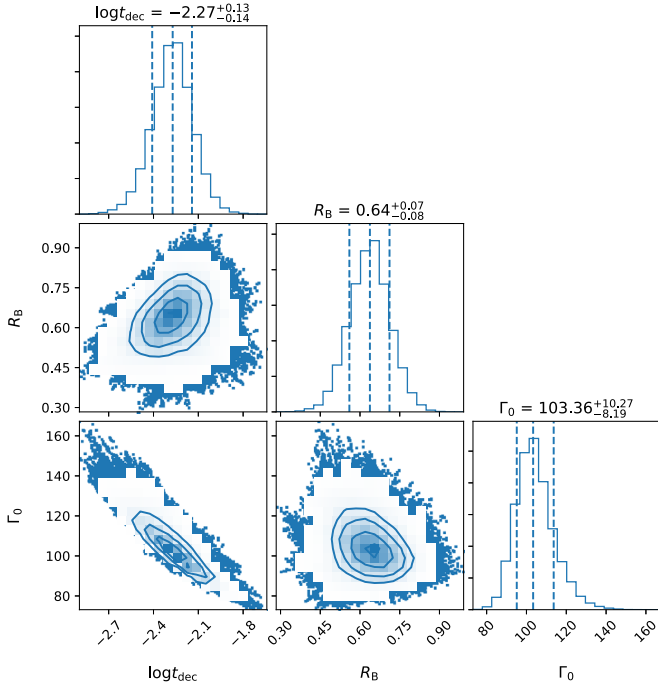
Figure 10. Correlations and marginalized posterior density functions for the deceleration time (t_{dec}) and relative magnetization ($R_B \equiv (\epsilon_{B,r}/\epsilon_{B,f})^{1/2}$) from the RS–FS consistency argument (Equation (4)), and the jet initial Lorentz factor (Γ_0), derived using energy balance (Equation (8)).

Table 4
FS and RS Model Parameters

Parameter	Best Fit	MCMC[a]
Forward Shock		
p	2.11	2.11 ± 0.01
$\log \epsilon_e$	−0.43	$-0.39^{+0.12}_{-0.17}$
$\log \epsilon_B$	−2.01	$-2.20^{+0.42}_{-0.78}$
$\log A_*$	−1.72	$-1.66^{+0.23}_{-0.13}$
$\log(E_{K,iso}/\text{ erg})$	53.3	$53.41^{+0.13}_{-0.16}$
$\log(A_V/\text{ mag})$	−1.83	$-1.84^{+0.14}_{-0.18}$
$\log \nu_{a,f}$ (Hz)	7.74[b]	...
$\log \nu_{m,f}$ (Hz)	12.7	...
$\log \nu_{c,f}$ (Hz)	16.4	...
$\log F_{\nu,m,f}$ (mJy)	0.62	...
Reverse Shock		
$\log(\nu_{a,r}/\text{ Hz})$	12.1	12.11 ± 0.06
$\log(\nu_{m,r}/\text{ Hz})$	8.6	$8.64^{+1.01}_{-0.45}$
$\log(\nu_{c,r}/\text{ Hz})$	14.7	$14.65^{+0.25}_{-0.22}$
$\log(F_{\nu,m,r}/\text{ mJy})$	5.2	$5.16^{+0.26}_{-0.56}$
g	2.72	$2.74^{+0.38}_{-0.31}$

Notes. Frequencies and flux densities are calculated at 1 day (FS) and 10^{-2} days (RS).
[a] Summary statistics from the marginalized posterior density distributions, with median and $\pm 34.1\%$ quantiles (corresponding to $\pm 1\sigma$ for Gaussian distributions; Figure 9).
[b] This frequency is not directly constrained by the data.

48 days after the burst. The corresponding radio maps were dynamic range limited, with noise dominated by image deconvolution errors. Thus, it is possible that our reported uncertainties underestimate the true variation of the non-Gaussian
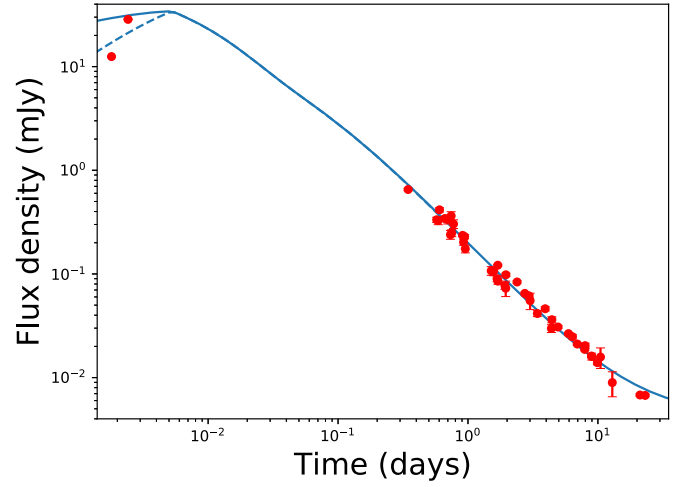
Figure 11. Optical light curve at r'/R and clear-band light curve of GRB 181201, together with an FS model with energy injection at $\lesssim t_{dec}$ at the rate expected for a shell at a uniform Lorentz factor, Γ_0, $E \propto t$ (solid) and at an enhanced rate of $E \propto t^{1.8}$ (dashed). The steep optical rise observed with MASTER suggests rapid energy injection into the FS during the deceleration stage (Section 5.1).
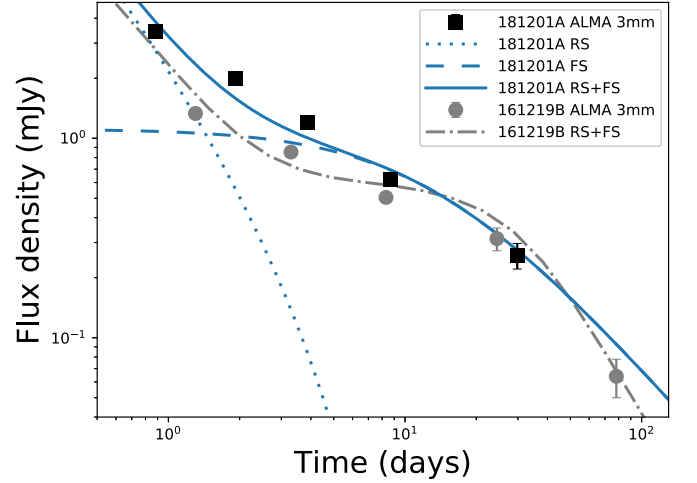
Figure 12. ALMA 3 mm light curve of GRB 181201A (black squares) compared with that of GRB 161219B (gray circles; Laskar et al. 2018a), together with RS+FS models (lines). Both GRBs exhibit excess millimeter-band emission near the RS–FS transition, indicating additional physics not captured by the model.

image noise. In that scenario, the light curve may be consistent with being flat and therefore host dominated. We caution that while a similar brightening is evident in the GMRT 750 MHz observations, they appear to be absent at 620 MHz. The two bands were observed together as part of a broader frequency coverage with the upgraded GMRT (GWB) system, and no systematic errors are expected in the light curve produced from different parts of the observing band.

On the other hand, we note that late-time light-curve flattenings or rebrightenings have been observed in several radio afterglows (Berger et al. 2003a; Panaitescu & Kumar 2004; Alexander et al. 2017; Laskar et al. 2018a, 2018b). If real, the rebrightening in this event might indicate (i) late-time energy injection due to slower ejecta shells[30] (Sari & Mészáros 2000; Kathirgamaraju et al. 2016), which has been

---

[30] The Lorentz factor of the FS is $\Gamma \approx 10$ at 40 days.

inferred in several instances (Laskar et al. 2015, 2018a, 2018c), or (ii) interaction of the FS with the wind termination shock, a scenario discussed above in the context of the X-ray light-curve flattening (Section 5.3). Any contribution from the emerging supernova is expected to peak on $\gtrsim 10$ yr timescales and therefore an unlikely explanation for this excess (Barniol Duran & Giannios 2015). The emergence of a counterjet, such as has been claimed in centimeter-band observations of GRB 980703 at $\gtrsim 500$ days after the burst (Li & Song 2004; Perley et al. 2017) should occur at $\gtrsim t_{\rm NR} \approx 220$ yr for this event (Section 5.3) and is also disfavored.

5.5. Are We Really Seeing the Reverse Shock?

We note that our derived value of $g \approx 2.7$, while higher than the theoretically expected upper limit for a wind environment (Zou et al. 2005), is comparable to $g \approx 2.3$ in GRB 140304A (Laskar et al. 2015). Previous studies have found even higher values of $g \approx 5$ in the case of the RS emission from GRB 130427A (Laskar et al. 2013; Perley et al. 2014). Higher values of g result in a more slowly evolving spectrum and are preferred by the fit due to the relatively slowly evolving centimeter/millimeter emission observed in these events, including in the event studied here. Owing to this mismatch with the theoretical prediction for g, as well as some of the other issues described above, it is natural to ask whether the RS +FS model is the only one that can explain the observations. It is possible that the emission observed here and in similar events in the past, which has been ascribed to the RS, is in fact from a different emission mechanism.

One possible alternate explanation is to invoke a two-component jet, one in which the optical and X-ray emission arises from a narrower, faster jet than that producing the centimeter-band observations (Berger et al. 2003c; Peng et al. 2005; Oates et al. 2007; Racusin et al. 2008; Holland et al. 2012). In such a case, we expect the radio peak frequency and peak flux density to evolve according to the standard FS prescription as $\nu_{\rm m} \propto t^{-3/2}$ and $F_{\nu,\rm m} \propto t^{-1/2}$, respectively. From the SED at 3.9 days (Section 3.1 and Figure 1), this would imply an R-band peak at $\approx 2.2 \times 10^{-3}$ days with a flux density of ≈ 60 mJy. While this would overpredict the MASTER observations at $\approx 2.4 \times 10^{-2}$ days, if the jet producing this emission component were still decelerating at this time, then the flux could be significantly lower. Furthermore, we find that this component would not contribute significantly to the remainder of the optical light curve. For instance, at the time of the earliest UVOT observation at ≈ 0.18 days, the predicted flux density of ≈ 0.2 mJy is below the observed flux density of ≈ 0.6 mJy. Whereas it is not possible for us to confirm or rule out two-component jet models, we note that decoupling the centimeter/millimeter emission from the optical/X-ray emission reduces the predictive power of such a model.

Another alternate scenario to explain the radio spectral bump at 3.9 days is the presence of a population of non-accelerated ("thermal") electrons, which are not accelerated by the passage of the FS into a relativistic power-law distribution, but instead form a Maxwellian distribution at lower energies (Eichler & Waxman 2005). However, a disjoint spectral component such as that observed here would likely require a very specific electron distribution, one in which the typical Lorentz factor of the thermal electrons is much lower than the minimum Lorentz
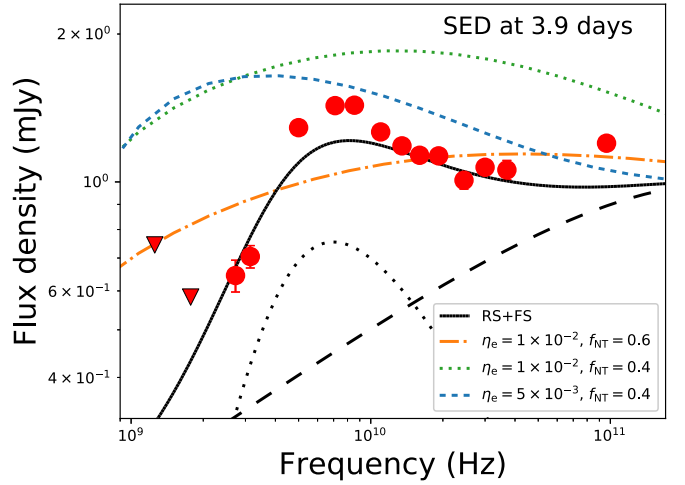

Figure 13. SED at 3.9 days (data points), with our best-fit model (solid, black) decomposed into FS (dashed) and RS (dotted) components, compared with a model incorporating thermal electrons (orange dashed–dotted, blue short dashes, and green dotted). The thermal electron model cannot easily match the sharp spectral peak observed in the centimeter band.

factor of the shock-accelerated electrons, the so-called "cold electron model" (Ressler & Laskar 2017).

The emission signature from such a population is expected to be quite broad. We demonstrate this by setting the electron participation fraction, usually assumed to be unity, to $f_{\rm NT} \approx 0.6$, and computing the resultant spectrum as described in Ressler & Laskar (2017). We use a cold electron model, with the ratio of electron temperature ($T_{\rm e}$) to gas temperature ($T_{\rm g}$) set at $\eta_{\rm e} \equiv T_{\rm e}/T_{\rm g} \approx 10^{-2}$. The resultant spectrum exhibits a broad peak in the centimeter band and does not match the observations as well as the RS model (Figure 13). While increasing $f_{\rm NT}$ increases the sharpness of the peak (relative to the underlying FS emission), doing so also increases the relative brightness of the thermal bump beyond the data, and so no combination of $f_{\rm NT}$ and $\eta_{\rm e}$ appears to match the centimeter-band data. A more detailed analysis requires a complete parameter search over $f_{\rm NT}$ and $\eta_{\rm e}$ that also includes the FS parameters. Such a study is currently not possible due to the computational intensiveness of the thermal electron calculation, and we defer it to future work.

5.6. FS Parameter Degeneracies

Our modeling reveals degeneracies between the FS model parameters (Figure 9), which cannot be explained by the unknown value of $\nu_{\rm a,f}$ alone. For instance, the correlation contours between A_* and $E_{\rm K,iso}$ lie parallel to the degenerate line $E_{\rm K,iso} \propto A_*^{1.4}$. However, the expected relation between these parameters when $\nu_{\rm a}$ is unknown is $E_{\rm K,iso} \propto A_*^{-0.2}$ (Granot & Sari 2002; Laskar et al. 2014). We note that the Compton Y parameter varies by about two orders of magnitude along the axis of the observed degeneracy, and thus the change in the physical parameters is compensated for by varying Y.

Our prescription for calculating Compton Y relies on a simplistic global approximation (Sari & Esin 2001; Laskar et al. 2015). However, we note that in low-density environments, the KN suppression limits the maximum value of Y (Nakar et al. 2009). We derive an expression for this maximum value of Y corresponding to the Lorentz factor of cooling electrons in a wind environment by substituting Equation (18)

from Panaitescu & Kumar (2000) for the effective density as a function of observer time in Equation (64) from Nakar et al. (2009) for the maximum value of Y when KN corrections are included to obtain

$$Y_{max}(\gamma_c) = 10 e^{\frac{27(3.2-p)^2-17}{(p+2)(4-p)}} e^{\left(\frac{8-p}{2(p+2)}\ln 0.73\right)}$$
$$\times \epsilon_{e,-1}^{\frac{5(p-1)}{p+2}} E_{53}^{\frac{p-3}{p+2}} A_*^{\frac{8-p}{p+2}} t_{days}^{-\frac{(2p-1)}{(p+2)}}. \quad (9)$$

For our best-fit parameters (Table 4), this evaluates to $Y_{max}(\gamma_c) \approx 2 t_{days}^{-0.8}$, which is lower than some of the values in the degenerate models discussed. Thus, a future, more accurate calculation incorporating KN corrections may resolve this source of degeneracy.

5.7. Burst Energetics and Radiative Efficiency

The data do not reveal a jet break (Rhoads 1999; Sari et al. 1999), and hence the degree of collimation remains unknown for this burst. As of the time of writing, we are continuing VLA observations of this event and expect that late-time observations may allow for beaming-independent calorimetry provided the contribution from the underlying host is negligible (Frail et al. 2000; Berger et al. 2003c, 2004; Frail et al. 2005; Shivvers & Berger 2011; De Colle et al. 2012). With that said, we note that our modeling does require some host contribution at 2.7–24.5 GHz at the $\approx 50\,\mu$Jy level (Figure 5), corresponding to a star formation rate of $\approx 2\,M_\odot\,\mathrm{yr}^{-1}$ (Yun & Carilli 2002; Berger et al. 2003a); hence, it is not clear whether such calorimetry will be feasible for this burst. For a jet break time of $t_{jet} \gtrsim 163$ days, we can only set a lower limit to the jet half-opening angle of $\theta_{jet} \gtrsim 6°$, corresponding to a minimum beaming-corrected energy of 1.4×10^{52} erg.

The radiative efficiency, on the other hand, is independent of the beaming correction. For our best-fit model, we find $\eta_{rad} \approx 0.35$. This value corresponds to a slightly lower efficiency than for other GRBs at similar $E_{\gamma,iso}$ as derived from X-ray afterglow observations (Lloyd-Ronning & Zhang 2004). However, the observed distribution of η_{rad} for *Swift* GRBs spans a broad range (Berger et al. 2003b; Nousek et al. 2006; Zhang et al. 2007; Beniamini et al. 2015), and this value of η_{rad} is unremarkable.

5.8. Low Circumburst Density

There is a strong observed correlation between multiwavelength detections of RS emission with low-density circumburst environments, typically $n_0, A_* \lesssim 10^{-2}$ (Laskar et al. 2018a). We note that the circumburst density for our best-fit model, $A_* \approx 0.02$, is also similarly low. We have previously remarked on the possibility that this is an observational selection effect, because low-density environments are more likely to result in a slow-cooling RS with long-lasting emission (Laskar et al. 2013, 2016, 2018a, 2019; Kopac et al. 2015; Alexander et al. 2017). In the case of GRB 161219B, we used constraints on the RS cooling frequency to determine a maximal particle density for the ISM environment under which RS emission was expected and showed that the observed density satisfied the constraint in that case. We repeat that argument here, now for the wind medium.

Combining Equation (2) with the expression for FS cooling frequency from Granot & Sari (2002),

$$\nu_{c,f} = 4.40 \times 10^{10}(3.45-p)e^{0.45p}(1+z)^{-3/2}$$
$$\times \epsilon_B^{-3/2} A_*^{-2} E_{K,iso,52}^{1/2} (1+Y_f)^{-2} t_d^{1/2}\,\mathrm{Hz}$$
$$\approx 10^{13} A_*^{-2}\,\mathrm{Hz}$$
$$\sim R_B^3 \nu_{c,r} \quad (10)$$

for the best-fit parameters at $t \approx 1$ days yields

$$A_* \approx \left(\frac{\nu_{c,r}}{10^{13}\,\mathrm{Hz}}\right)^{-1/2} R_B^{-3/2}$$
$$\lesssim 0.24 R_B^{-3/2}\,\mathrm{cm}^{-3}, \quad (11)$$

which is indeed satisfied for GRB 181201A where $A_* \approx 2 \times 10^{-2}$ (corresponding to a mass-loss rate $\dot{M} \approx 2 \times 10^{-7}\,M_\odot\,\mathrm{yr}^{-1}$ for a wind speed of $10^3\,\mathrm{km\,s}^{-1}$). We note that a similar low wind parameter of $A_* \approx 3 \times 10^{-3}$ was inferred in the case of GRB 130427A, which also exhibited a strong RS signature (Laskar et al. 2013; Perley et al. 2014). Our observation of RS emission in GRB 181201A therefore supports the hypothesis that RS emission is more easily detectable in low-density environments, in both the ISM and wind scenarios.

5.9. Reverse-shock Lorentz Factor

During our analysis above, we have assumed a nonrelativistic RS. We now check this assumption by calculating the Lorentz factor of the RS itself. During the shock crossing, the Lorentz factor of the shocked fluid in the cold ejecta frame is given by

$$\bar{\gamma} \approx \frac{1}{2}\left(\frac{\Gamma_{FS}/\sqrt{2}}{\Gamma_0} + \frac{\Gamma_0}{\Gamma_{FS}/\sqrt{2}}\right), \quad (12)$$

where Γ_{FS} is the FS Lorentz factor, assumed to be highly relativistic. The RS Lorentz factor is then given by the shock jump condition (Blandford & McKee 1976)

$$\bar{\Gamma}_{RS} = \frac{(\bar{\gamma}+1)[\hat{\varsigma}(\bar{\gamma}-1)+1]^2}{\hat{\varsigma}(2-\hat{\varsigma})(\bar{\gamma}-1)+2}, \quad (13)$$

where we take the adiabatic index $\hat{\varsigma} = 4/3$, appropriate for a relativistic fluid (Kobayashi & Sari 2000). We compute these quantities from our MCMC results and find $\bar{\Gamma}_{RS} = 1.97_{-0.07}^{+0.08}$, corresponding to a shock speed of $\bar{\beta}_{RS} = 0.74 \pm 0.02$ and four-velocity $\bar{\Gamma}_{RS}\bar{\beta}_{RS} = 1.7 \pm 0.1$. Thus, the RS is at most mildly relativistic and definitely not ultrarelativistic ($\bar{\Gamma}_{RS}\bar{\beta}_{RS} \gg 1$). Whereas the expressions we have used for the RS evolution in the modeling are strictly valid only in the asymptotic regime of a Newtonian RS, they are expected to be approximately correct for cold shells where the postshock evolution deviates from the Blandford–McKee solution. A more detailed analysis requires numerical calculation of the RS hydrodynamics and radiation simultaneously with the MCMC fitting, which is beyond the scope of this work.

5.10. Ejecta Magnetization

The relative magnetization of $R_B \approx 0.6$ observed in this event is similar to $R_B \approx 1$ for GRB 161219B (Laskar et al. 2018a) and

$R_{\rm B} \approx 0.6$ for GRB 140304A (Laskar et al. 2018c). On the other hand, these values are all smaller than $1 \lesssim R_{\rm B} \lesssim 5$ for GRB 130427A (Laskar et al. 2013), $R_{\rm B} \approx 8$ for GRB 160509A (Laskar et al. 2016), $R_{\rm B} \sim 1$–100 for GRB 160509A (Alexander et al. 2017), and $R_{\rm B} \approx 1$–100 derived for GRBs with optical flashes (Gomboc et al. 2008, 2009; Japelj et al. 2014). Interpreting these values requires accounting for the variation in $\epsilon_{\rm B,f}$ between events, which we perform next.

The plasma magnetization in the ejecta, σ, defined as the ratio of the magnetic energy density to the rest-mass energy density, corresponds to $\sigma \approx \epsilon_{\rm B,r} \bar{\Gamma}_{\rm RS}$. For the nonrelativistic RSs observed in all of these cases, this implies $\sigma \approx \epsilon_{\rm B,r} = R_{\rm B}^2 \epsilon_{\rm B,f}$. A detailed statistical comparison of σ between GRBs requires full posterior density functions for $R_{\rm B}$ in each case, which are not currently available. However, we can use the typical parameters in each case for a rough comparison. For our best-fit parameters, we have $\epsilon_{\rm B,r} \approx 2.6 \times 10^{-3}$ for GRB 181201A. For GRB 160625B, the large feasible range of $R_{\rm B} \sim 1$–100 makes comparisons less meaningful. For GRB 160509A, $R_{\rm B}^2 \epsilon_{\rm B,f} > 1$; however, the RS in that case was long lived and continuously refreshed, thus suggesting additional physics not captured by the simple calculation of σ. For the other bursts with radio RS emission, we find $\epsilon_{\rm B,r} \approx 6 \times 10^{-2}$ (161219B), $\epsilon_{\rm B,r} \approx 2 \times 10^{-2}$ (140304A), and $\epsilon_{\rm B,r} \approx 0.2 - 1$ (130427A). Thus, for all GRBs with detected and well-constrained RS emission, σ ranges between 10^{-3} and ≈ 1, indicating that the ejecta are weakly magnetized. However, we caution that this outcome is largely built into the formalism for nonrelativistic RSs, for which $\sigma \approx \epsilon_{\rm B,r}$. The multiwavelength detection and characterization of a relativistic RS might enable us to explore a broader regime in σ.

In summary, the detection of the RS signature in this GRB argues against the scenario where the jet is Poynting flux dominated, as in that case, no RS emission is expected (Lyutikov & Camilo Jaramillo 2017). The mildly relativistic RS observed in this case argues against propagation in a highly magnetized, relativistic outflow, such as in a magnetar wind (Metzger et al. 2011). This event brings the number of GRBs with radio RS detections to seven (Kulkarni et al. 1999; Sari & Piran 1999a; Laskar et al. 2013, 2016, 2018a, 2018c, 2019; Perley et al. 2014; Alexander et al. 2017).

6. Conclusions

We have presented multiwavelength radio to X-ray observations of GRB 181201A spanning from $\approx 150\,{\rm s}$ to ≈ 163 days after the burst. We have modeled these observations in the standard afterglow synchrotron emission framework to derive the burst energetics and parameters of the explosion. The radio data we present reveal the presence of an additional component, which we interpret as emission from electrons heated by a mildly relativistic ($\bar{\Gamma}_{\rm RS} \approx 2$) RS that propagates through the ejecta in $t_{\rm dec} \approx 460\,{\rm s}$. We have performed detailed, self-consistent modeling of the RS and FS to derive the initial Lorentz factor, $\Gamma = 103^{+10}_{-8}$, and magnetization, $R_{\rm B} \equiv B_{\rm RS}/B_{\rm FS} = 0.64^{+0.07}_{-0.08}$, of the jet that produced this gamma-ray burst. The low inferred ejecta magnetization disfavors a Poynting-flux-dominated outflow. The derived low circumburst density is consistent with the emerging requirement of low-density environments for long-lasting, detectable RS emission to be produced. The MCMC analysis performed here explores degeneracies between the RS and FS parameters for the first time and can be used to derive the

properties of the ejecta and surrounding environment. We have explored deviations of the data from the proposed model, including a steep early optical rise, an excess in the millimeter band on intermediate timescales, and a late-time excess in the X-ray and radio emission, and placed these observations in the context of similar signatures observed in other events. Detailed multifrequency observations and modeling of GRBs followed by a summative sample study may provide greater insight into the origin of these deviations. Our results reveal additional degeneracies in the FS parameters due to an incomplete treatment of inverse-Compton cooling; future work that incorporates the KN corrections may help alleviate this problem, allowing for even better constraints on the underlying physical processes and central engine responsible for GRBs and their afterglows.

ORCID iDs

Tanmoy Laskar ⓘ https://orcid.org/0000-0003-1792-2338
Hendrik van Eerten ⓘ https://orcid.org/0000-0002-8680-8718
Patricia Schady ⓘ https://orcid.org/0000-0002-1214-770X
C. G. Mundell ⓘ https://orcid.org/0000-0003-2809-8743
Kate D. Alexander ⓘ https://orcid.org/0000-0002-8297-2473
Edo Berger ⓘ https://orcid.org/0000-0002-9392-9681
J. Bolmer ⓘ https://orcid.org/0000-0002-3373-0646
Ryan Chornock ⓘ https://orcid.org/0000-0002-7706-5668
Deanne L. Coppejans ⓘ https://orcid.org/0000-0001-5126-6237
Wen-fai Fong ⓘ https://orcid.org/0000-0002-7374-935X
Shiho Kobayashi ⓘ https://orcid.org/0000-0001-7946-4200
Raffaella Margutti ⓘ https://orcid.org/0000-0003-4768-7586
Re'em Sari ⓘ https://orcid.org/0000-0002-1084-3656
Ryo Yamazaki ⓘ https://orcid.org/0000-0002-1251-7889
V. M. Lipunov ⓘ https://orcid.org/0000-0003-3668-1314
R. Rebolo ⓘ https://orcid.org/0000-0003-3767-7085
M. Serra-Ricart ⓘ https://orcid.org/0000-0002-2394-0711

References

Akerlof, C., Balsano, R., Barthelmy, S., et al. 1999, Natur, 398, 400
Alexander, K. D., Laskar, T., Berger, E., et al. 2017, ApJ, 848, 69
Amati, L. 2006, MNRAS, 372, 233
Arimoto, M., Axelsson, M., & Ohno, M. 2018, GCN, 23480, 1
Barniol Duran, R., & Giannios, D. 2015, MNRAS, 454, 1711
Beniamini, P., Nava, L., Duran, R. B., & Piran, T. 2015, MNRAS, 454, 1073
Berger, E., Cowie, L. L., Kulkarni, S. R., et al. 2003a, ApJ, 588, 99
Berger, E., Kulkarni, S. R., & Frail, D. A. 2003b, ApJ, 590, 379
Berger, E., Kulkarni, S. R., & Frail, D. A. 2004, ApJ, 612, 966
Berger, E., Kulkarni, S. R., Pooley, G., et al. 2003c, Natur, 426, 154
Blandford, R. D., & McKee, C. F. 1976, PhFl, 19, 1130
Bradley, L., Sipocz, B., Robitaille, T., et al. 2016, Photutils: Photometry Tools v0.7, Astrophysics Source Code Library, ascl:1609.011
Burrows, D. N., Hill, J. E., Nousek, J. A., et al. 2005, SSRv, 120, 165
Chandra, P., Cenko, S. B., Frail, D. A., et al. 2008, ApJ, 683, 924
Chevalier, R. A., & Li, Z.-Y. 2000, ApJ, 536, 195
De Colle, F., Ramirez-Ruiz, E., Granot, J., & Lopez-Camara, D. 2012, ApJ, 751, 57
Eichler, D., & Waxman, E. 2005, ApJ, 627, 861
Figer, D. F., McLean, I. S., & Morris, M. 1999, ApJ, 514, 202
Fong, W., Berger, E., Metzger, B. D., et al. 2014, ApJ, 780, 118
Foreman-Mackey, D., Hogg, D. W., Lang, D., & Goodman, J. 2013, PASP, 125, 306
Frail, D. A., Kulkarni, S. R., Nicastro, L., Feroci, M., & Taylor, G. B. 1997, Natur, 389, 261
Frail, D. A., Soderberg, A. M., Kulkarni, S. R., et al. 2005, ApJ, 619, 994
Frail, D. A., Waxman, E., & Kulkarni, S. R. 2000, ApJ, 537, 191
Gat, I., van Eerten, H., & MacFadyen, A. 2013, ApJ, 773, 2
Gomboc, A., Kobayashi, S., Guidorzi, C., et al. 2008, ApJ, 687, 443
Gomboc, A., Kobayashi, S., Mundell, C. G., et al. 2009, in AIP Conf. Ser. 1133, ed. N. G. C. Meegan & C. Kouveliotou (Melville, NY: AIP), 145
Granot, J., & Königl, A. 2003, ApJL, 594, L83
Granot, J., & Sari, R. 2002, ApJ, 568, 820
Granot, J., & Taylor, G. B. 2005, ApJ, 625, 263
Holland, S. T., De Pasquale, M., Mao, J., et al. 2012, ApJ, 745, 41
Izzo, L., de Ugarte Postigo, A., Kann, D. A., et al. 2018, GCN, 23488, 1

Japelj, J., Kopač, D., Kobayashi, S., et al. 2014, ApJ, 785, 84
Kathirgamaraju, A., Barniol Duran, R., & Giannios, D. 2016, MNRAS, 461, 1568
Khanam, T., Sharma, V., Vibhute, A., et al. 2018, GCN, 23501, 1
Kobayashi, S. 2000, ApJ, 545, 807
Kobayashi, S., Piran, T., & Sari, R. 1999, ApJ, 513, 669
Kobayashi, S., & Sari, R. 2000, ApJ, 542, 819
Kobayashi, S., & Zhang, B. 2007, ApJ, 655, 973
Kong, A. K. H. 2018, GCN, 23475, 1
Kopac, D., Mundell, C. G., Kobayashi, S., et al. 2015, ApJ, 806, 179
Krühler, T., Küpcü Yoldas, A., Greiner, J., et al. 2008, ApJ, 685, 376
Kulkarni, S. R., Frail, D. A., Sari, R., et al. 1999, ApJL, 522, L97
Laskar, T., Alexander, K. D., Berger, E., et al. 2016, ApJ, 833, 88
Laskar, T., Alexander, K. D., Berger, E., et al. 2018a, ApJ, 862, 94
Laskar, T., Alexander, K. D., Gill, R., et al. 2019, ApJL, 878, L26
Laskar, T., Berger, E., Chornock, R., et al. 2018b, ApJ, 858, 65
Laskar, T., Berger, E., Margutti, R., et al. 2015, ApJ, 814, 1
Laskar, T., Berger, E., Margutti, R., et al. 2018c, ApJ, 859, 134
Laskar, T., Berger, E., Tanvir, N., et al. 2014, ApJ, 781, 1
Laskar, T., Berger, E., Zauderer, B. A., et al. 2013, ApJ, 776, 119
Li, Z., & Song, L. M. 2004, ApJL, 614, L17
Liang, E.-W., Racusin, J. L., Zhang, B., Zhang, B.-B., & Burrows, D. N. 2008, ApJ, 675, 528
Liang, E.-W., Yi, S.-X., Zhang, J., et al. 2010, ApJ, 725, 2209
Lipunov, V., Kornilov, V., Gorbovskoy, E., et al. 2010, AdAst, 2010, 349171
Lipunov, V. M., Vladimirov, V. V., Gorbovskoi, E. S., et al. 2019, ARep, 63, 293
Lloyd-Ronning, N. M., & Zhang, B. 2004, ApJ, 613, 477
Lyutikov, M., & Camilo Jaramillo, J. 2017, ApJ, 835, 206
Margutti, R., Guidorzi, C., Lazzati, D., et al. 2015, ApJ, 805, 159
Martini, P., Stoll, R., Derwent, M. A., et al. 2011, PASP, 123, 187
McMahon, E., Kumar, P., & Piran, T. 2006, MNRAS, 366, 575
McMullin, J. P., Waters, B., Schiebel, D., Young, W., & Golap, K. 2007, in ASP Conf. Ser. 376, Astronomical Data Analysis Software and Systems XVI, ed. R. A. Shaw, F. Hill, & D. J. Bell (San Francisco, CA: ASP), 127
Melandri, A., Kobayashi, S., Mundell, C. G., et al. 2010, ApJ, 723, 1331
Mereghetti, S., Gotz, D., Ferrigno, C., et al. 2018, GCN, 23469, 1
Mészáros, P. 2006, RPPh, 69, 2259
Mészáros, P., & Rees, M. J. 1993, ApJ, 405, 278
Mészáros, R., & Rees, M. J. 1997, ApJ, 482, 29
Mészáros, P., & Rees, M. J. 1999, MNRAS, 306, L39
Metzger, B. D., Giannios, D., Thompson, T. A., Bucciantini, N., & Quataert, E. 2011, MNRAS, 413, 2031
Mimica, P., & Giannios, D. 2011, MNRAS, 418, 583
Molinari, E., Vergani, S. D., Malesani, D., et al. 2007, A&A, 469, L13
Nakar, E., Ando, S., & Sari, R. 2009, ApJ, 703, 675
Nakar, E., & Piran, T. 2004, MNRAS, 353, 647
Nousek, J. A., Kouveliotou, C., Grupe, D., et al. 2006, ApJ, 642, 389
Oates, S. R., de Pasquale, M., Page, M. J., et al. 2007, MNRAS, 380, 270
Panaitescu, A., & Kumar, P. 2000, ApJ, 543, 66
Panaitescu, A., & Kumar, P. 2004, MNRAS, 350, 213
Peng, F., Königl, A., & Granot, J. 2005, ApJ, 626, 966
Perley, D. A., Cenko, S. B., Corsi, A., et al. 2014, ApJ, 781, 37
Perley, D. A., Hjorth, J., Tanvir, N. R., & Perley, R. A. 2017, MNRAS, 465, 970
Podesta, R., Lopez, C., Podesta, F., et al. 2018, GCN, 23470, 1
Poole, T. S., Breeveld, A. A., Page, M. J., et al. 2008, MNRAS, 383, 627
Racusin, J. L., Karpov, S. V., Sokolowski, M., et al. 2008, Natur, 455, 183
Rees, M. J., & Mészáros, P. 1992, MNRAS, 258, 41P
Rees, M. J., & Mészáros, P. 1994, ApJL, 430, L93
Ressler, S. M., & Laskar, T. 2017, ApJ, 845, 150
Rhoads, J. E. 1999, ApJ, 525, 737
Roming, P. W. A., Kennedy, T. E., Mason, K. O., et al. 2005, SSRv, 120, 95
Sari, R., & Esin, A. A. 2001, ApJ, 548, 787
Sari, R., & Mészáros, P. 2000, ApJL, 535, L33
Sari, R., & Piran, T. 1999a, ApJL, 517, L109
Sari, R., & Piran, T. 1999b, ApJ, 520, 641
Sari, R., Piran, T., & Halpern, J. P. 1999, ApJL, 519, L17
Sari, R., Piran, T., & Narayan, R. 1998, ApJL, 497, L17
Schlafly, E. F., & Finkbeiner, D. P. 2011, ApJ, 737, 103
Shao, L., & Dai, Z. G. 2007, ApJ, 660, 1319
Shivvers, I., & Berger, E. 2011, ApJ, 734, 58
Siegel, M. H., & Cannizzo, J. K. 2018, GCN, 23499, 1
Steele, I. A., Smith, R. J., Rees, P. C., et al. 2004, Proc. SPIE, 5489, 679
Svinkin, D., Golenetskii, S., Aptekar, R., et al. 2018, GCN, 23495, 1
Troja, E., Lipunov, V. M., Mundell, C. G., et al. 2017, Natur, 547, 425

16

Usov, V. V. 1992, Natur, 357, 472
van der Horst, A. J., Paragi, Z., de Bruyn, A. G., et al. 2014, MNRAS, 444, 3151
Vurm, I., Hascoët, R., & Beloborodov, A. M. 2014, ApJL, 789, L37
Waxman, E., Kulkarni, S. R., & Frail, D. A. 1998, ApJ, 497, 288
Woosley, S. E., & Bloom, J. S. 2006, ARA&A, 44, 507

Yun, M. S., & Carilli, C. L. 2002, ApJ, 568, 88
Zhang, B., & Kobayashi, S. 2005, ApJ, 628, 315
Zhang, B., Kobayashi, S., & Mészáros, P. 2003, ApJ, 595, 950
Zhang, B., Liang, E., Page, K. L., et al. 2007, ApJ, 655, 989
Zou, Y. C., Wu, X. F., & Dai, Z. G. 2005, MNRAS, 363, 93